A ground-based instrument suite for integrated high-time resolution measurements of pulsating aurora with Arase

K. Hosokawa[1], S.-I. Oyama[2,3,4], Y. Ogawa[3], Y. Miyoshi[2], S. Kurita[5], M. Teramoto[6], S. Nozawa[2], T. Kawabata[2], Y. Kawamura[1], Y.-M. Tanaka[3], H. Miyaoka[3], R. Kataoka[3], K. Shiokawa[2], U. Brändström[7], E. Turunen[8], T. Raita[8], M. Johnsen[9], C. Hall[9], D. Hampton[10], B. Kozelov[11], A. Demekov[11], Y. Ebihara[5], Y. Kasahara[12], S. Matsuda[13], I. Shinohara[13], and R. Fujii[14]

[1] Graduate School of Communication Engineering and Informatics, University of Electro-Communications, Chofugaoka, Chofu, Tokyo, Japan.

[2] Institute for Space-Earth Environmental Research, Nagoya University, Furo-cho, Chikusa-ku, Nagoya, Aichi, Japan.

[3] National Institute of Polar Research, Midori-cho, Tachikawa, Tokyo, Japan

[4] University of Oulu, Pentti Kaiteran katu, Linnanmaa, Oulu, Finland

[5] Research Institute for Sustainable Humanosphere, Kyoto University, Gokasho, Uji, Kyoto, Japan

[6] Kyushu Institute of Technology, Sensuicho, Tobata-ku, Fukuoka, Japan

[7] The Swedish Institute of Space Physics, Rymdcampus, Kiruna, Sweden

[8] Sodankylä Geophysical Observatory, Tähteläntie, Sodankylä, Finland

[9] Tromsø Geophysical Observatory, UiT The Arctic University of Norway, Tromsø, Norway

[10] Geophysical Institute, University of Alaska Fairbanks, Fairbanks, Alaska, USA

[11] Polar Geophysical Institute, Apatity, Murmansk, Russia

[12] Graduate School of Natural Science and Technology, Kanazawa University, Kakuma-machi, Kanazawa, Ishikawa, Japan

[13] Institute of Space and Astronautical Science, Yoshinodai, Chuo-ku, Sagamihara, Kanagawa, Japan

[14] Research Organization of Information and Systems, Toranomon, Minato-ku, Tokyo, Japan

For submission to *Journal of Geophysical Research - Space Physics*

Correspondence: Keisuke Hosokawa (keisuke.hosokawa@uec.ac.jp)

Key points:

1. An integrated package of instruments for high-time resolution measurements of pulsating aurora was deployed in Scandinavia and Alaska
2. The system has enabled us to capture the fine-scale spatio-temporal variations of pulsating aurora in a wide area
3. Data from those instruments have also been used for simultaneous observations of pulsating aurora with the Arase satellite

Abstract

A specialized ground-based system has been developed for simultaneous observations of pulsating aurora (PsA) and related magnetospheric phenomena with the Arase satellite. The instrument suite is composed of 1) six 100-Hz sampling high-speed all-sky imagers (ASIs), 2) two 10-Hz sampling monochromatic ASIs observing 427.8 and 844.6 nm auroral emissions, 3) Watec Monochromatic Imagers, 4) a 20-Hz sampling magnetometer and 5) a 5-wavelength photometer. The 100-Hz ASIs were deployed in four stations in Scandinavia and two stations in Alaska, which have been used for capturing the main pulsations and quasi 3 Hz internal modulations of PsA at the same time. The 10-Hz sampling monochromatic ASIs have been operative in Tromsø, Norway with the 20-Hz magnetometer and the 5-wavelength photometer. Combination of these multiple instruments with the European Incoherent SCATter (EISCAT) radar enables us to reveal the energetics/electrodynamics behind PsA and further to detect the low-altitude ionization due to energetic electron precipitation during PsA. In particular, we intend to derive the characteristic energy of precipitating electrons during PsA by comparing the 427.8 and 844.6 nm emissions from the two monochromatic ASIs. Since the launch of

the Arase satellite, the data from these instruments have been examined in comparison with the wave and particle data from the satellite in the magnetosphere. In the future, the system will be utilized not only for studies of PsA but also for other categories of aurora in close collaboration with the planned EISCAT_3D project.

1. Introduction

Pulsating aurora (PsA) is a common aurora phenomenon often observed during the recovery phase of auroral substorms (see recent reviews by Lessard, 2012; Hosokawa et al., 2015; Nishimura et al., 2020). In general, PsA is produced by intermittent precipitations of a few keV to a few tens of keV electrons caused by the pitch angle scattering in the magnetosphere (Miyoshi et al., 2010, 2015a; Nishiyama et al., 2011). Chorus and ECH waves have been considered as strong candidates contributing to this wave-particle interaction process (Nishimura et al., 2010; Fukizawa et al., 2018). Recent magnetospheric observations by the Arase satellite (Miyoshi et al., 2018a) demonstrated that chorus waves actually cause PsA through scattering of energetic electrons into the loss cone (Kasahara et al., 2018) and determined the temporal variations of PsA (Ozaki et al., 2019, Hosokawa et al., 2020). Nakajima et al. (2012) have suggested some waves other than chorus and ECH waves may also contribute to cause PsA at higher latitudes.

One of the unique characteristics of PsA, that are different from other types of aurora, is its complicated temporal variations. The temporal variation of PsA is known to consist of two distinct periodicities. One is the “main pulsation” in the timescale from a few to a few tens of seconds which is observed for all the cases of PsA (e.g., Yamamoto, 1988). The other is much faster modulations, which are often called “internal modulations” or “quasi 3 Hz modulations”. These sub-second variations are embedded within the ON

phase of the main pulsation (Sandahl et al., 1980). The internal modulations are observed in many cases of PsA, but their appearance is known to depend on MLT (Røyrvik and Davis, 1977).

Miyoshi et al. (2015a) proposed a model explaining the origins of two periodicities of PsA (i.e., main pulsation and internal modulations) considering the characteristics of wave-particle interactions with chorus. They suggested that repetitive bursts of chorus (chorus bursts), which appear every few seconds, cause the main pulsation of PsA, while rising tone chorus elements embedded in a chorus burst produce electron precipitation responsible for the internal modulations (Rosenberg et al., 1971; Foster and Rosenberg, 1976). Recently, this model has been successfully tested by simultaneous conjugate observations of PsA from the ground and chorus waves by the Arase satellite in the magnetosphere. Kasahara et al. (2018) demonstrated that the chorus bursts induced pitch angle scattering of tens of keV electrons into the loss cone and subsequently caused PsA. Later, Hosokawa et al. (2020) showed two sets of one-to-one correspondence, one between the main pulsations of PsA and chorus bursts and the other between the internal modulations and rising tone chorus elements. Hosokawa et al. (2020) also indicated that PsA without the internal 3 Hz modulations is caused by chorus bursts without discrete elements (i.e., hiss-like emissions). The chorus elements are suggested to grow efficiently due to a nonlinear effect (Nunn, 1974; Roux and Pellat, 1978; Katoh and Omura, 2007; Omura et al., 2008; Omura et al., 2013). According to the combined global MHD and advection simulation, the chorus waves can grow efficiently due to the nonlinear effect from the pre-midnight to pre-noon region (Ebihara et al., 2020). This characteristic spatial distribution is consistent with that of PsA (Røyrvik and Davis, 1977), which supports the causal link between chorus and PsA.

High-time resolution optical observations in the last decade discovered further faster modulations whose frequency is higher than 10 Hz. For example, Samara and Michell (2010) identified 12-Hz modulations in the time-series of PsA. Kataoka et al. (2012) showed ~54-Hz modulations in the data from a high-speed camera. Although there have been a few reports about these fast modulations, it still remains an open question what processes produce such faster modulations beyond 10 Hz. One of the possible origins of these faster modulations of PsA is the so-called "subpacket" structure embedded within a single element of chorus (Foster et al., 2017). The subpacket structure is considered to be formed by repetitive saturations of nonlinear wave growth (e.g., Omura et al., 2019), which could be a key process for characterizing the temporal evolution of chorus waves. Continuous (i.e., routine) high-speed optical observations capable of capturing these rapid phenomena, especially in conjunction with chorus wave observations in the magnetosphere, are essential to understand the process controlling the entire temporal variation of PsA including the modulations beyond 10 Hz.

PsA is known to show various shapes and motions. Recently, Grono and Donovan (2018, 2020) claimed that amorphous type PsA shows characteristics that are different from typical patch-type or arc-type PsA. Such studies of spatial characteristics of PsA imply that generation mechanisms may depend on the morphology (or behavior) of PsA. Nishiyama et al. (2016) demonstrated the existence of sub-patch structures within a patch of PsA using the principal component analysis. They showed that each sub-patch has a different variation, suggesting the importance of two-dimensional optical observations for discriminating the characteristics of sub-patch structures.

THEMIS-GBO (Time History of Events and Macroscale Interactions during Substorms - Ground-Based Observatory) successfully observed the dynamics of aurora

in a wide area in North America (Mende et al., 2008). However, the temporal resolution of the ASIs of THEMIS-GBO, that is 3 s, was not always sufficient to observe both the main pulsation and internal modulation of PsA; thus, it has still been difficult to reveal the full spectrum of PsA periodicity in a wide area. To overcome this limitation, we intended to develop an instrument package for observations of PsA, which can be a high-time resolution version of THEMIS-GBO although the coverage is limited compared to THEMIS-GBO at this stage. As summarized in the earlier part of this section, there are three distinct periodicities in the time-series of PsA: 1) main pulsation (a few to a few tens of second), 2) internal modulations (~3 Hz), and 3) faster modulation (> 10 Hz). In order to detect all of these variations, it is needed to install high-time resolution ASIs, whose temporal resolution is, for example, 100 Hz.

In the past, several high-time resolution optical observations were carried out (e.g., Kataoka et al., 2012). Most of these measurements were, however, campaign-based observations at a single station. In addition, those previous observations employed a camera with a narrow field-of-view (FOV). One of the big differences between those previous observations and our observation is that we operate high-speed "all-sky" imagers at multiple locations in Scandinavia and Alaska in a "routine" manner. This will allow us not only to visualize the sub-second variations of PsA in 2D in a wide area, but also to carry out a statistical analysis of the characteristics of PsA based on a large amount of data from the routine high-time resolution measurements.

As described above, it has been known that PsA has a broad impact on the ionosphere and middle atmosphere. In this sense, in addition to the wide coverage of the optical observations, it is also demanded to conduct integrated and comprehensive observations by combining ground-based radio and optical observations. For this purpose,

we deployed two monochromatic ASIs, a 5-channel photometer and a high-time resolution ground-based magnetometer in Tromsø, Norway where the EISCAT radar is operative. Data from the monochromatic ASIs and the photometer can be used to estimate the characteristics energy of precipitating electrons following methods introduced, for instance, by Ono (1993) and Lanchester et al. (1994). In particular, it would be possible to derive a map of the average energy of PsA electrons by using the all-sky images from the monochromatic ASIs. Such more quantitative optical data in combination with observations of EISCAT and the newly deployed ground-based magnetometer will enable us to understand the impact of PsA on the atmosphere and the ionospheric electrodynamics.

As mentioned in the first part of the introduction section, simultaneous satellite observations of the chorus wave in the magnetosphere are indispensable for understanding the generation mechanism of PsA. For this purpose, we intended to conduct several campaign observations of PsA by using the newly deployed ground-based instruments in Scandinavia and Alaska with the Arase satellite launched in Dec 2016 (Miyoshi et al., 2018a). To take a full advantage of the limited opportunities to conduct simultaneous observations, it is needed to deploy the high-speed ASIs into as many as possible locations. We have installed the ASIs into 6 stations in the auroral region and contributed to enhance the ground-based coverage for the simultaneous ground-satellite observations. In this report, we introduce the technical detail of the instruments and demonstrate how data from these instruments have been used for studies of PsA in combination with observations of Arase and the the EISCAT radar.

2. Instruments

2.1. 100-Hz ASI observations

The 100-Hz all-sky imager (ASI) is composed of an EMCCD (Electron Multiplying Charge-Coupled Device) camera of Hamamatsu Photonics (C9100-23B) and C-mount fish-eye lens of Fujinon Co. Ltd (FE185C086HA-1). The fish-eye lens is directly attached to the aperture of the EMCCD camera. An optical filter is installed above the lens, which will be described in the later part of this section. The camera begins capturing images by responding to external triggers given 100 times per second (i.e., 100 Hz). The EMCCD camera has an imaging part whose resolution is 512 x 512 pixels. Before sending out from the camera, however, the images are binned with 2 x 2 windows and the spatial resolution of the final output images turns out to be 256 x 256 pixels. The images are transferred from the camera to the Personal Computer (PC) by using a camera control software and saved to the internal solid state drive (SSD). When the images are saved to data files, 6000 images obtained during a 1 min interval are compiled and stored in a single “raw format” file with 16-bit depth.

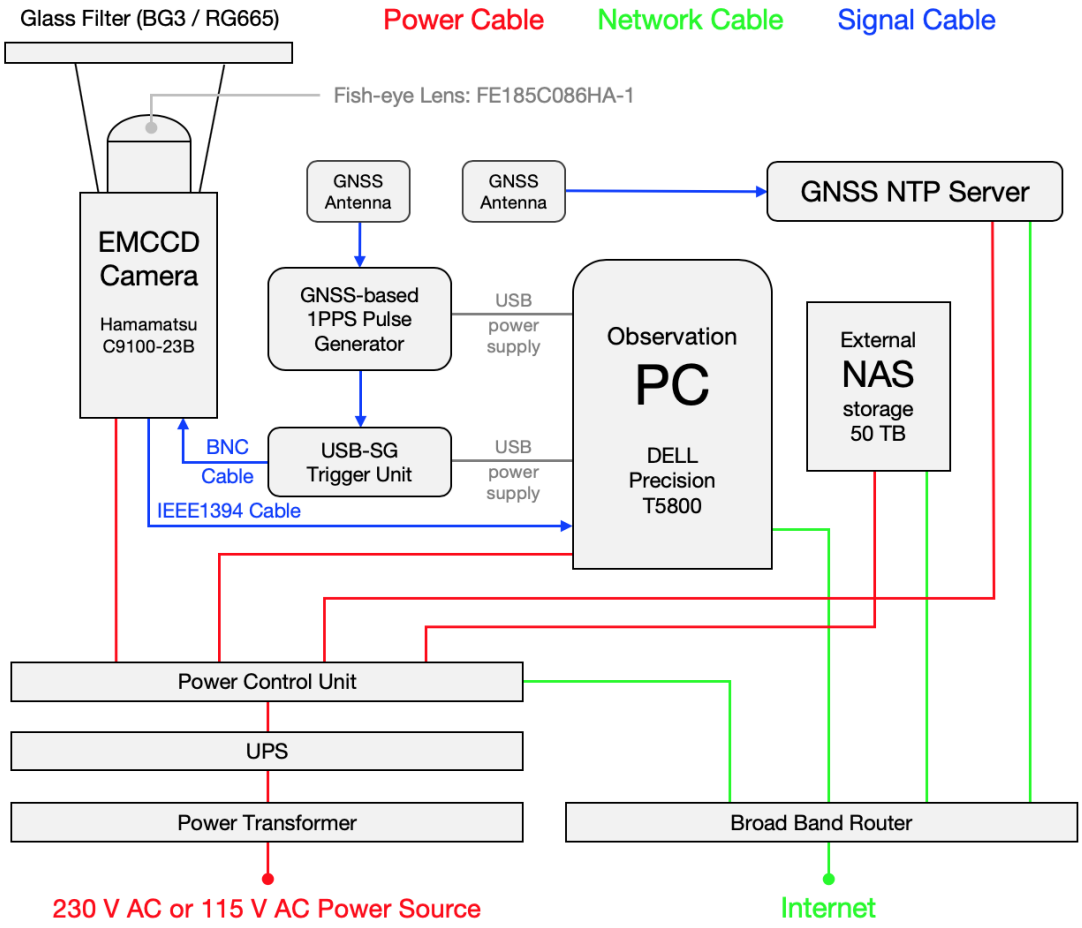

Figure 1: Block diagram of the 100-Hz ASI system.

Figure 1 shows a block diagram of the entire system of the 100-Hz sampling ASI. As mentioned above, the camera is externally triggered by a USB signal generator (USB-SG trigger unit) which produces 100 pulses per second responding to a trigger by GNSS-based 1PPS pulse generator. The camera is directly connected to the PC with an IEEE1394 cable, and the images can be captured and saved without significant image losses. On average, image loss may happen approximately once every 100,000 sampling. We automatically run the camera from the beginning of astronomical twilight in the evening to the end of astronomical twilight in the next morning (when the Sun is below the horizon by -12 degrees) independent of the Moon phase.

The clock of the PC is adjusted every minute using the GNSS NTP server prepared within the local private network. The accuracy of the clock of the PC is as large as a few msec which is less than the sampling interval of the ASI. The size of the raw data for a 1-min interval is 750 MB. The raw data files are stored in the local SSD drive, whose size is 1 TB, during the nighttime observation, and then copied to the external NAS storage during the daytime. The observations in the winter season normally start at the beginning of September and finish in the end of March. During the operational period, due to the limitation of the onsite NAS storage, we only keep good data obtained when the local weather condition was good and aurora activity was identified, using the quick look data at https://ergsc.isee.nagoya-u.ac.jp/psa-gnd/bin/psa.cgi.

To capture the rapid temporal variation of PsA, especially sub-second internal modulations, it is needed to cut the slower auroral emission lines out. For example, the emission at 557.7 nm is known to have a systematic delay due to the finite lifetime of $O(^1S)$ excited state of oxygen atom (~0.7 sec) and that at 630.0 nm is known to show much longer delay of ~110 sec again due to the lifetime of $O(^1D)$ state (e.g., Jones, 1974). Unless we do remove the contribution of these slower emissions, it is difficult to associate the rapid modulation of PsA, such as internal modulations (~3 Hz) and further faster ones, with fine-scale temporal variations in chorus waves at the magnetospheric counterpart. For this purpose, we considered to use wideband optical filters, i.e., RG665 and BG3, both of which are so-called glass filters. The BG3 glass filter was first employed for measurements of aurora with an EMCCD camera by Samara et al. (2012). They demonstrated that the use of the filter increased the intensity variation of rapid modulation of PsA only by a few percent. As mentioned above, however, we intended to associate the chorus observations by the Arase satellite with the rapid optical variations of PsA;

thus, any undesired delays from the electron precipitation to the optical emission needs to be removed. For this reason, we decided to use these glass filters for the current 100-Hz ASI observations.

We put the glass filter on top of the fish-eye lens and succeeded in removing most of the contributions of 557.7 nm and 630.0 nm emissions. Figure 2 shows the transmission characteristics of the RG665 (orange) and BG3 (purple) glass filters. Transmission of both the filters can cut the 557.7 nm and 630.0 nm lines, yet passes prompt emissions. In the first year of measurement, we employed the RG665 filter at all the stations. As shown in Figure 2, the RG665 glass filter covers prompt emissions of nitrogen molecules extending from 650 to 700 nm (so-called N_2 1PG Bands depicted by the gray vertical lines). However, there is still a small contribution from the O(^{1}D) emission at 630.0 nm. Since the start of the second winter season from September 2017, we have been using the BG3 filter which completely removes the contribution of 630.0 nm. In this case, one of the main components is the so-called N_2^+ 1NG emission at 427.8 nm (blue vertical line in Figure 2). But, the BG3 filter is also able to capture several prompt emissions of N_2 1PG existing in near-infrared areas from 700 to 800 nm since the quantum efficiency of the EMCCD camera is still ~70% at 800 nm.

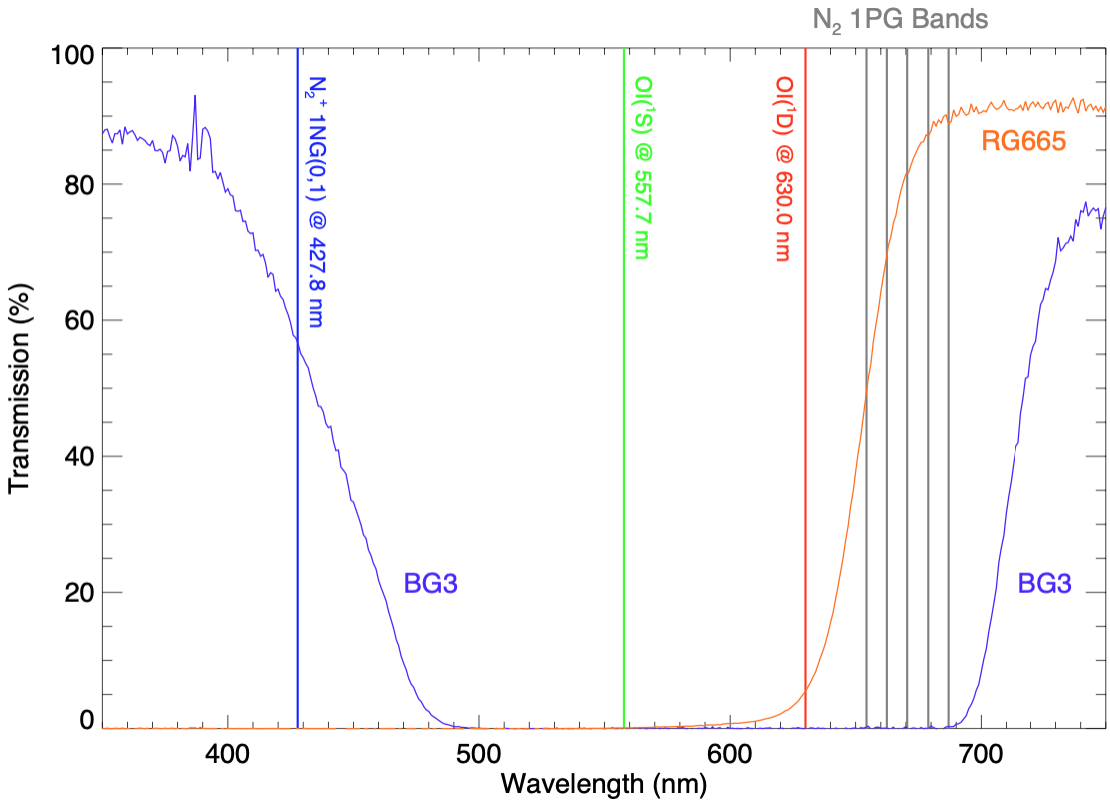

Figure 2: Transmission characteristics of the RG665 (orange) and BG3 (purple) glass filters used for the 100-Hz ASI observations. Several auroral emission lines are overplotted for comparison.

We have installed the 100-Hz ASIs in 4 places in Scandinavia and 2 places in Alaska. The ASIs in Kevo, Gakona and Poker Flat were deployed by a joint effort with the PWING project (Shiokawa et al., 2017). The locations (i.e., geographic latitude, geographic longitude and magnetic latitude: MLAT) of the entire 6 stations are summarized in Table 1. Figure 3 shows the field-of-view (FOV) of these ASIs in the geographic coordinate system with an assumption of emission altitude at 110 km, where the contours of AACGM magnetic latitude (Baker and Wing, 1989) are overplotted. In both the panels, the statistical location of the auroral oval for Kp = 4 is superimposed (Feldstein and Starkov, 1967). As shown in Figure 3a, the FOVs of the 4 EMCCD ASIs

in Tromsø, Kevo, Tjautjas and Sodankylä, whose FOVs are depicted respectively by the 4 red circles, construct a seamless network of optical observations covering from 15° to 35° in longitude and 64° to 73° in latitude. In particular, the ASIs cover the equatorward part of the statistical auroral oval where frequent appearance of PsA is expected.

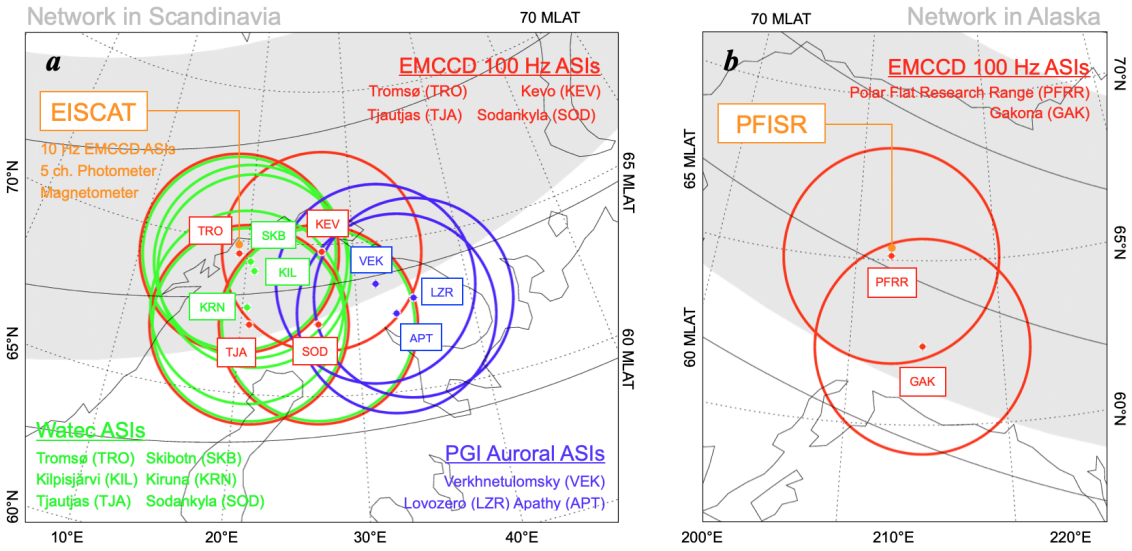

Figure 3: Fields-of-view of the ASIs **(a)** in the Scandinavian sector and **(b)** in Alaskan sector. The contours of AACGM magnetic latitude (Baker and Wing, 1989) are overplotted. In both the panels, the auroral oval modeled by Feldstein and Starkov (1967) is depicted for Kp = 4 case.

As will be introduced later in this section, we deployed several other ground-based equipments in Scandinavia. For example, two 10-Hz monochromatic ASIs, a 5-channel photometer and a magnetometer have been operative in Tromsø, which enables us to carry out simultaneous observations of common auroral phenomena by using multiple instruments including the EISCAT radar. In addition, 6 sets of the Watec ASIs were installed in Tromsø, Skibotn, Kilpisjarvi, Tjautjas, Sodankylä and Kiruna (Ogawa et al., 2020a) which increases the coverage of optical observations and also provides capability of monitoring the appearance of aurora in real-time. There are several other ASIs in the

westernmost part of Russia, in the Kola Peninsula, which are operated by the Polar Geophysical Institute (PGI) (Kozelov et al., 2012, Roldugin et al., 2017). The FOVs of these ASIs shown by the blue circles in Figure 3a well overlap the viewing area of the EMCCD ASIs in Finland (Kevo and Sodankylä); thus, the combination of these Russian ASIs further extends the coverage of the network to the eastern side of Scandinavia.

In Alaska, we have been operating two 100-Hz sampling EMCCD ASIs in Gakona and Poker Flat. As shown in Figure 3b, the FOVs of these two ASIs cover a region extending in the latitudinal direction (from 59 to 69 MLAT) including the viewing area of the Poker Flat Incoherent Scatter Radar (PFISR). The coverage of the ASI in Gakona extends down to 59 MLAT, which enables us to observe optical manifestation of microbursts in the subauroral latitudes.

2.2 10-Hz ASI observations

In addition to the 100-Hz sampling high-speed ASIs, we have been operating two monochromatic all-sky cameras at the EISCAT radar facility in Tromsø, which are equipped with narrow band-pass optical filters for observing specific aurora emissions. The purpose of this monochromatic observation is to derive the characteristic energy of precipitating electrons from the intensity of two auroral emission lines. Since we need to observe optical emissions in much narrower wavelength, i.e., the incoming flux of photons is much more limited compared to that of the 100-Hz ASIs, the exposure time and corresponding temporal resolution (sampling interval) become longer, which have been 10-Hz for the monochromatic ASIs. This 10-Hz exposure time was determined by considering the longest interval that can detect the internal modulation of PsA, which is normally 3 Hz. The system is composed of two identical ASIs equipped with different

optical filters. The ASI-2 optics of Nikon developed by Taguchi et al. (2004) are combined with the same EMCCD cameras (C9100-23B of Hamamatsu Photonics). The EMCCD cameras capture an image when it is externally triggered. These external triggering pulses are delivered from a USB-SG trigger directly connected to the PC. The camera captures 100-msec exposure images 10 times in a second. Since the exposure time of this monochromatic observation is 10 times longer than that of the 100-Hz high-speed ASIs, the USB-SG is triggered by the control PC once a minute and the USB-SG triggers the camera 1000 times following a trigger from the PC (i.e., 10 times in a second). The image capturing/saving procedure is the same as that of the 100-Hz ASIs, but the size of one raw file compiling 600 images (256 x 256 pixels) in a minute is only 75 MB.

There are several auroral emissions that can be used for estimating the energy of precipitating electrons, for example, 427.8 nm, N_2 1PG between 650-700 nm, 777.4 nm and 844.6 nm (e.g., Ono 1993; Lanchester et al., 1994). The basic idea is that we estimate the characteristic energy of precipitating electrons by using the ratio of emission intensities at two different wavelengths. If we consider a pair of emissions at 427.7 nm and 844.6 nm, the N_2^+ 1NG emission at 427.8 nm is mainly caused by relatively harder electron precipitation while the oxygen emission at 844.6 nm is more associated with soft electrons; thus, the ratio of 427.8 nm emission to that of 844.6 nm emission can be used as a proxy for the characteristic energy of incoming electrons. This two wavelengths method has been used by many studies such as Ono (1993) and Lanchester et al. (1994).

The emissions we have considered are 427.8 nm, N_2 1PG (650-700 nm), 777.4 nm and 844.6 nm emissions. All of these emissions are prompt emission; thus, we do not need to consider any time delays of the emission from the collisional excitation by the auroral electrons. When we started the 10-Hz monochromatic ASI observations, we did

not know which pair of the emissions is the best combination to be used for the energy estimation. Then, we operated four identical monochromatic ASIs in the same place (in Tromsø) and tried to determine the best pair of the emissions for estimating the energy of PsA electrons. The results are described in detail in Oyama et al. (2018), but it was found that the emission at 777.4 nm, which was originally considered as an emission representing low-energy component of PsA precipitation, can also be produced by relatively harder precipitations. This means that the use of 777.4 nm is not appropriate for the two wavelength method. The N_2 1PG band emission extending from 650 to 700 nm is composed of 5 bands in this range, and the emission model of GLOW (Solomon et al., 2017) is not able to model these wavelengths. By considering these factors, we eventually decided to use 427.8 nm as a proxy for the harder precipitation and 844.6 nm as that for softer precipitation. Selection of optical filters for the 10-Hz monochromatic ASIs in Tromsø are summarized in Table 1. As mentioned above, we tested 777.4 nm and N_2 1PG emission during the first season from September 2016 to April 2017. Since the beginning of the second winter season from September 2017, we have only observed 427.8 and 844.6 nm emissions.

Table 1: Geographic and magnetic coordinates (AACGM) of the 6 stations in Scandinavia and Alaska. The settings (selection of optical filter and sampling rate) of the instruments are also given.

Station (ID)	Instruments			
Operation period	High Speed ASI	Monochromatic ASI	Photometer	Magnetometer
Tromsø, Norway (TRO)	Glat: 69.58, Glon: 19.23, MLAT: 66.76			
20160925 to 20170126		10 Hz @ 427.8 nm as Cam5 10 Hz @ 777.4 nm as Cam1 10 Hz @ 844.6 nm as Cam3		20 Hz sampling
20170128 to 20170416	100 Hz @ RG665 as Cam1	10 Hz @ 427.8 nm as Cam5 10 Hz @ N2 1PG as Cam4 10 Hz @ 844.6 nm as Cam3	20 Hz sampling	
20170902 -	100 Hz @ BG3 as Cam1	10 Hz @ 427.8 nm as Cam5 10 Hz @ 844.6 nm as Cam3	400 Hz sampling	
Sodankylä, Finland (SOD)	Glat: 67.37, Glon: 26.63, MLAT: 64.19			
20160926 to 20170423	100 Hz @ RG665 as Cam2			
20170918 -	100 Hz @ BG3 as Cam2			
Tjautjas, Sweden (TJA)	Glat: 67.31, Glon: 20.73, MLAT: 64.39			
20170906 -	100 Hz @ BG3 as Cam4			
Kevo, Finland (KEV)	Glat: 69.76, Glon: 27.01, MLAT: 66.57			
20170129 to 20170415	100 Hz @ RG665 as Cam6			
20170831 -	100 Hz @ BG3 as Cam6			
Gakona, Alaska, USA (GAK)	Glat: 62.39, Glon: 214.78, MLAT: 63.32			
20170304 to 20170503	100 Hz @ RG665 as Cam7			
20170928 -	100 Hz @ BG3 as Cam7			
Pokar Flat, Alaska, USA (PFRR)	Glat: 65.13, Glon: 212.51, MLAT: 65.65			
20180830 -	100 Hz @ BG3 as Cam8			

The procedure for deriving the absolute optical intensity (in Rayleigh: R) is based on a method described in Ogawa et al. (2020a). Following the procedure introduced in Ogawa et al. (2020a), we have obtained calibration images by using an integrating sphere for optical calibration which was available in National Institute of Polar Research (Ogawa et al., 2020b). We took calibration images for all the configurations employed in the observation. During the observation, we set the sensitivity (EMGAIN) value of the EMCCD camera to be 200 (EMGAIN can range from 0 to 255), which enabled us to capture dim emissions of 427.8 nm and 844.6 nm with an exposure time of 100 ms.

Figure 4 shows an example of the calibration process for the 427.8 nm emission with EMGAIN = 200 setting. The top four panels show calibration images taken for four levels of source light intensities of the integrating sphere from 0.25 x 10^{-6} W sr^{-1} m^{-2} nm^{-}

^{1} to 1.0 x 10^{-6} W sr^{-1} m^{-2} nm^{-1}. Figure 4e is a so-called “dark image” taken when putting the lens cap on the optics (i.e., no incidence of light). Note that the contribution of these dark counts has already been subtracted in the calibration images in Figures 4a-d. These “dark count subtracted raw count” values are likely to have an almost linear relationship with the source light intensity (i.e., the raw count becomes larger as the source light intensity increases).

Figure 4f shows the relationship between the integrated light intensity in the unit of Rayleigh [R] in the horizontal axis and the raw count including the dark count in the vertical axis. Here we considered the spectrum of the light source and transmission characteristics of the optical filter to derive the integrated light intensity in the units of [R]. Note that, in this figure, we plot the data at 6 pixels in the images which are indicated by the colored circles (red one at the center and blue one near the edge of the FOV). At all the sampled pixels, there is a reasonable linear correlation, which allows us to derive a map of sensitivity [count R^{-1}] as an inclination of the fitted linear slope function. It is also possible to estimate the dark count as an intercept of the vertical axis in Figure 4f.

Figures 4g and 4h respectively show the map of sensitivity and dark count obtained by carrying out the above estimation at all the 256 x 256 pixels in the image. The sensitivity value is about 0.5 count R^{-1} which means that 1 raw count corresponds to ~2 R. We applied the same calibration procedure to the calibration images of 844.6 nm with EMGAIN = 200 setting. We save the estimated maps of dark image (Figure 4g) and sensitivity (Figure 4h) for both the emissions as calibration files and use them when converting the observed values of raw count to the absolute optical intensity in the units of R.

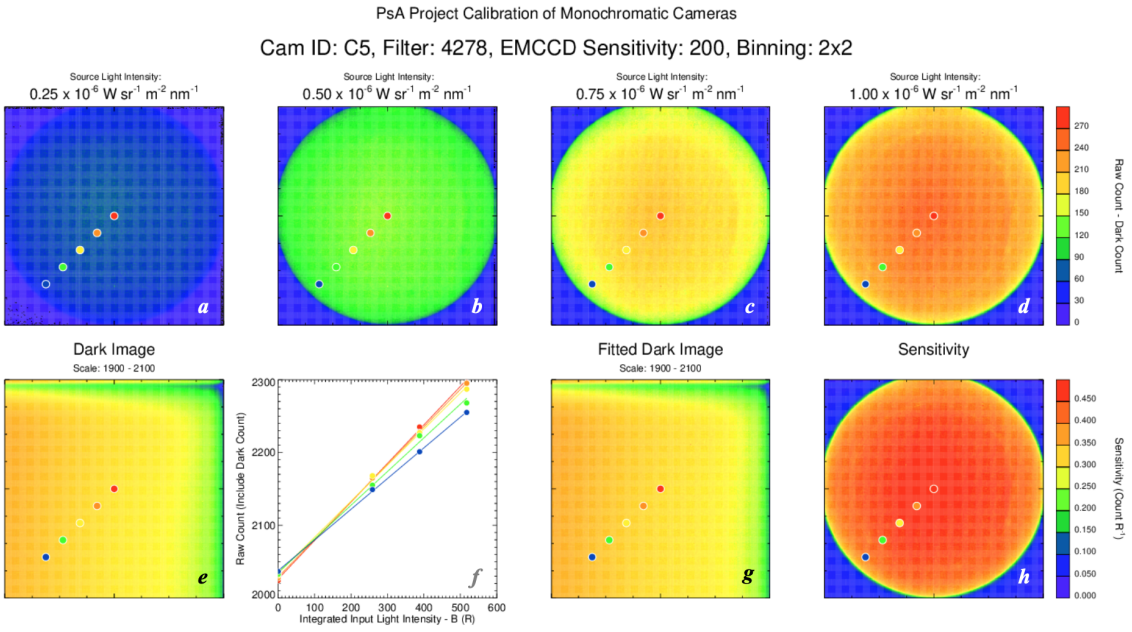

Figure 4: Calibration procedure of the monochromatic ASI for observing 427.8 nm emission with EMGAIN = 200 setting. **(a-d)** The top four panels show calibration images taken for four levels of source light intensities of the integrating sphere, **(e)** "dark image" taken when putting the lens cap on the optics, **(f)** relationship between the integrated light intensity in the unit of R in the horizontal axis and the raw count including the dark count in the vertical axis, **(g)** map of dark count, **(h)** map of sensitivity in the unit of count R^{-1}.

2.3 20-Hz fluxgate magnetometer observations

The 20-Hz magnetometer consists of a sensor, a GPS (Global Positioning System) receiver, a magnetometer electronics unit, and a PC. The dimensions of the magnetometer sensor part (MAG-03TB) developed by Bartington Instruments Ltd. are diameter of 280 mm and height of 110 mm. This magnetometer system can observe three orthogonal components of the geomagnetic field with a dynamic range of ± 70,000 nT and the resolution of less than 1 nT. The typical noise intensity at 1 Hz is 6 $pT/Hz^{1/2}$, and the mean square level of the noise is 0.2 nT p-p in the frequency band of 0.01-1 Hz. The GPS system with a time accuracy of less than ± 1μ sec provides 1PPS to the AD converter of the magnetometer and completely synchronizes the time stamp in the magnetometer data

with a resolution of 300 Hz. The DCA-500BA magnetometer electronics units made by TIERRA TECNICA Ltd. are equipped with Linux Arm11. The magnetometer data are stored in the internal flash memory with a sampling rate of 20 Hz and transferred to a data server in Japan once a day. We installed the magnetic field sensor in a small house and adjusted the X, Y, and Z components to northward, eastward, and downward directions, respectively. The sensor is connected to the magnetometer electronics units with a 70 m cable covered with plastic tubes. The magnetometer electronics units and the PC were installed in an observation building, in which the EMCCD ASIs are operative. The GPS receiver, which provides precise time information for the magnetometer, was mounted to the exterior wall of the main house.

2.4 Watec ASIs

For the studies of PsA, it is important to derive the average energy and flux of precipitating electrons in a quantitative manner by using ground-based imagers with monochromatic filters. For this purpose, all-sky Watec Monochromatic Imagers (WMIs) have been complementarily deployed at six locations in northern Scandinavia. The specifications and locations of the WMIs are summarized in Ogawa et al. (2020a). The fields-of-view of the WMIs at Tromsø, Skibotn, Kilpisjarvi, Kiruna, Tjautjas and Sodankylä are plotted with green circles in Figure 3a. By using the multi-wavelength data from WMIs with a temporal resolution of 1 sec, we are able to derive the energy of precipitating electrons during PsA not only in Tromsø, where the monochromatic EMCCD ASIs are operative, but also over a wide area in northern Scandinavia. The multi-wavelength data from WMIs at multiple stations can also be used for tomographic reconstruction of aurora structure because the FOVs of the WMI systems at Tromsø,

Skibotn, Kilpisjärvi and Kiruna have a significant overlap.

The data from WMI systems are also useful for real-time monitoring of the status of aurora in northern Scandinavia because the size of the WMI images is relatively small and the data can be transferred to Japan in a quasi real-time manner. To find suitable events for PsA studies, real-time WMI quick-look plots and archived WMI database have been maintained and available in the following web-pages: http://pc115.seg20.nipr.ac.jp/www/opt/index.html, and, http://pc115.seg20.nipr.ac.jp/www/AQVN/index.html

2.5 Photometer

A 5-channel photometer has also been operative in Tromsø since January 2017. This photometer observes 5 optical emissions (427.8 nm, 557.7 nm, 630.0 nm, 777.4 nm and 844.6 nm) in the field-aligned direction with a sampling rate of 400 Hz. The original 400 Hz data are normally down-sampled to 20 Hz and used to visualize the temporal variation of sub-second variations of PsA. The detailed description of the system can be found in Nozawa et al. (2018). One of the primary purposes of the deployment of the photometer is the calibration of two monochromatic EMCCD ASIs also operative at Tromsø. Since the deployment, the photometer was calibrated using an integrating sphere at National Institute of Polar Research once a year during summer months when the optical observations are resumed. The photometer data at 427.8 and 557.7 nm emissions were also employed to estimate the energy of PsA electrons (Kawamura et al., 2020).

3. Observations

3.1 Example of 100-Hz observations

Figure 5 shows an example of the multi-point observations of PsA from four EMCCD ASI stations (TRO, TJA, KEV and SOD) in Scandinavia which was obtained at 01:05 UT on March 15, 2018. To make this plot, we have integrated the original 100-Hz images with a sampling rate of 25 Hz to reduce the random noise typical in the low-light condition measurement with EMCCD cameras. It might be difficult to see only from this static image, but there are a number of patches of PsA within the FOVs of all the four ASIs. The latitudinal coverage of the combined FOV extends from 65 to 72 geographic latitude, which corresponds to an L value range from ~4.5 to almost 7.5. During the interval surrounding this image, we detected both the main pulsation and internal modulations at some of the stations, which enables us to investigate the latitudinal and longitudinal (i.e., MLT) dependence of the characteristics of the main pulsation and internal modulations.

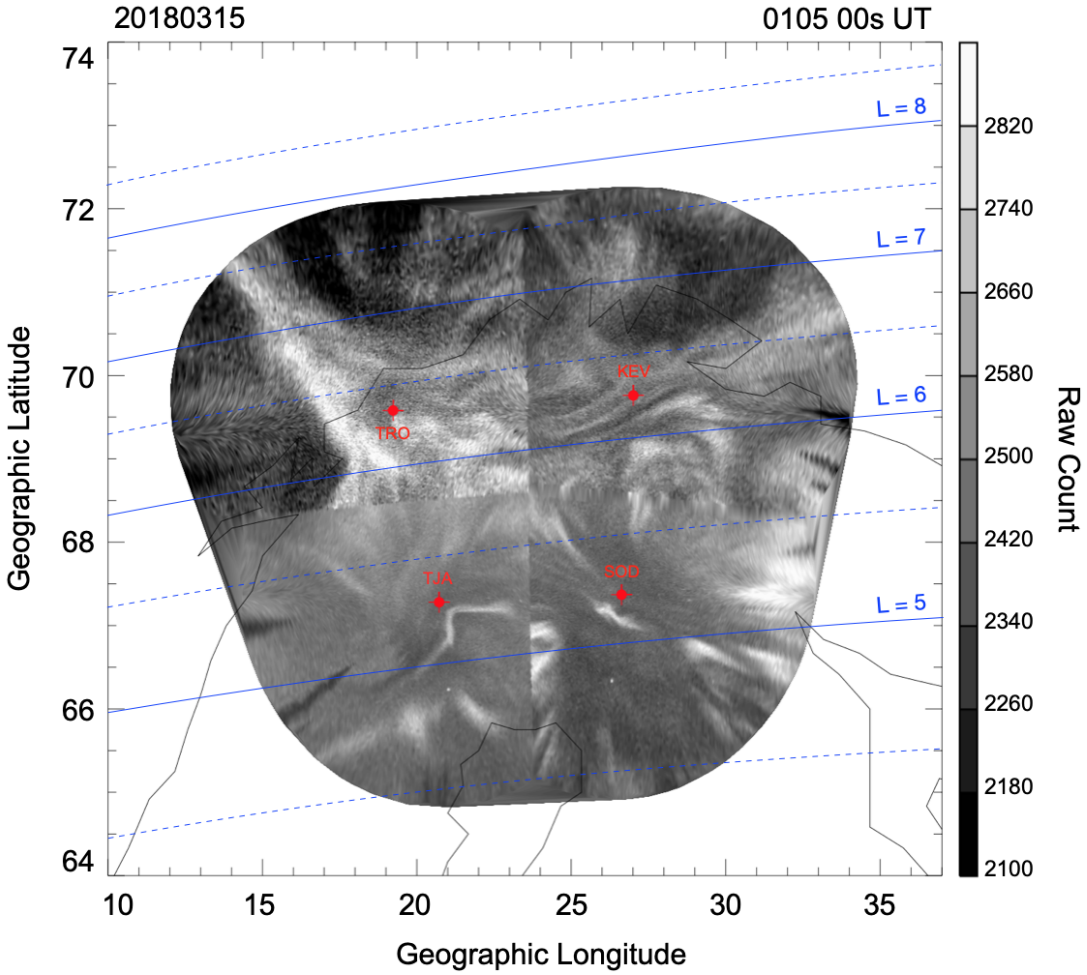

Figure 5: Example of the multi-point observations of PsA by the four 100-Hz sampling EMCCD ASIs in Scandinavia which was obtained at 01:05 UT on March 15, 2018.

A few previous ground-based observations suggested an occurrence of PsA showing shorter period (of main pulsation) at lower latitudes (Thomas and Rothwell, 1979; Duncan et al., 1981). These results were interpreted as the latitudinal difference in the bounce period of 2 keV electrons (Thomas and Rothwell, 1979). The data used in those studies, however, were clearly insufficient for statistical analyses. The wide latitudinal coverage of the current network observations in Scandinavia and Alaska provides us chances to revisit this problem by conducting statistics with sufficient data. Not only that, of course, we could reveal how the characteristics of internal modulation

can change with magnetic latitude. Røyrvik and Davis (1977) indicated by using a limited amount of all-sky TV camera observations that approximately 50% of PsAs display internal modulation. By examining the high-time resolution optical data in a wide area in a statistical fashion, we could reveal how the percentage of simultaneous appearance of main pulsation and internal modulation depends on magnetic latitude, which will provide a clue to understand the origin of main and ~3 Hz modulation of PsA.

As described in the introduction section, PsA is known to have two distinct periodicities which are “main pulsation” and “internal modulation”. Most of previous PsA studies have investigated the main pulsation, whose periodicity ranges from a few to a few tens of second, and discussed the correlation of those pulses with bursty appearances of chorus waves in the magnetosphere. The current observations aim at further understanding the relationship between the other periodicity of PsA, which is so-called internal modulation at ~3 Hz, and fine-scale structures embedded within chorus (i.e., chorus elements). For that purpose, it is indispensable to capture the internal modulation clearly. Figure 6 displays the temporal variations of PsA obtained by the 100-Hz ASI in Tjautjas, Sweden during the interval of simultaneous observations of PsA in Scandinavia on March 15, 2018 (Figure 5). Figure 6a is the time-series of optical data in a format of south to north keogram. The keogram is filled with a number of vertical stripes, most of which are signatures of the main pulsation. It is clearly seen that the apparent periodicity of the main pulsation is different at different time and latitudinal location. This makes it difficult to answer what determines the periodicity of the main pulsation.

Figure 6b is a zoom-in view of the 1-min optical data within the green box in the southern half of Figure 6a. In a region near the horizontal red line, 9 enhancements of optical intensity are seen, which are manifestations of the main pulsation. In this case, the

periodicity of the main pulsation is 6-10 sec. The zoom-in keogram also indicates an existence of short time-scale streaks embedded in the ON phase of the main pulsation. These very thin stripes are the signatures of internal (~3 Hz) modulation of PsA. Figure 6c shows two time-series of the raw count sampled along the red and blue lines in Figure 6b. It is clearly seen that there are several tiny peaks on the plateau of the main pulsation, which are the manifestation of the 3 Hz internal modulation. These data well demonstrate that the 100-Hz ASIs are able to detect the main pulsation (a few to a few tens of second) and the internal modulation (a few Hz) at the same time. In particular, the use of glass filters, that can remove the contamination of long-lived 557.7 and 630.0 nm emission, enabled us to observe prompt emissions only; thus, the signatures of internal modulation can be seen in the time-series. Such high-time resolution optical data from the network (6 ASIs) will contribute to detailed understanding of the latitudinal and longitudinal (MLT dependence) variations of the sub-second fine-scale characteristics of PsA.

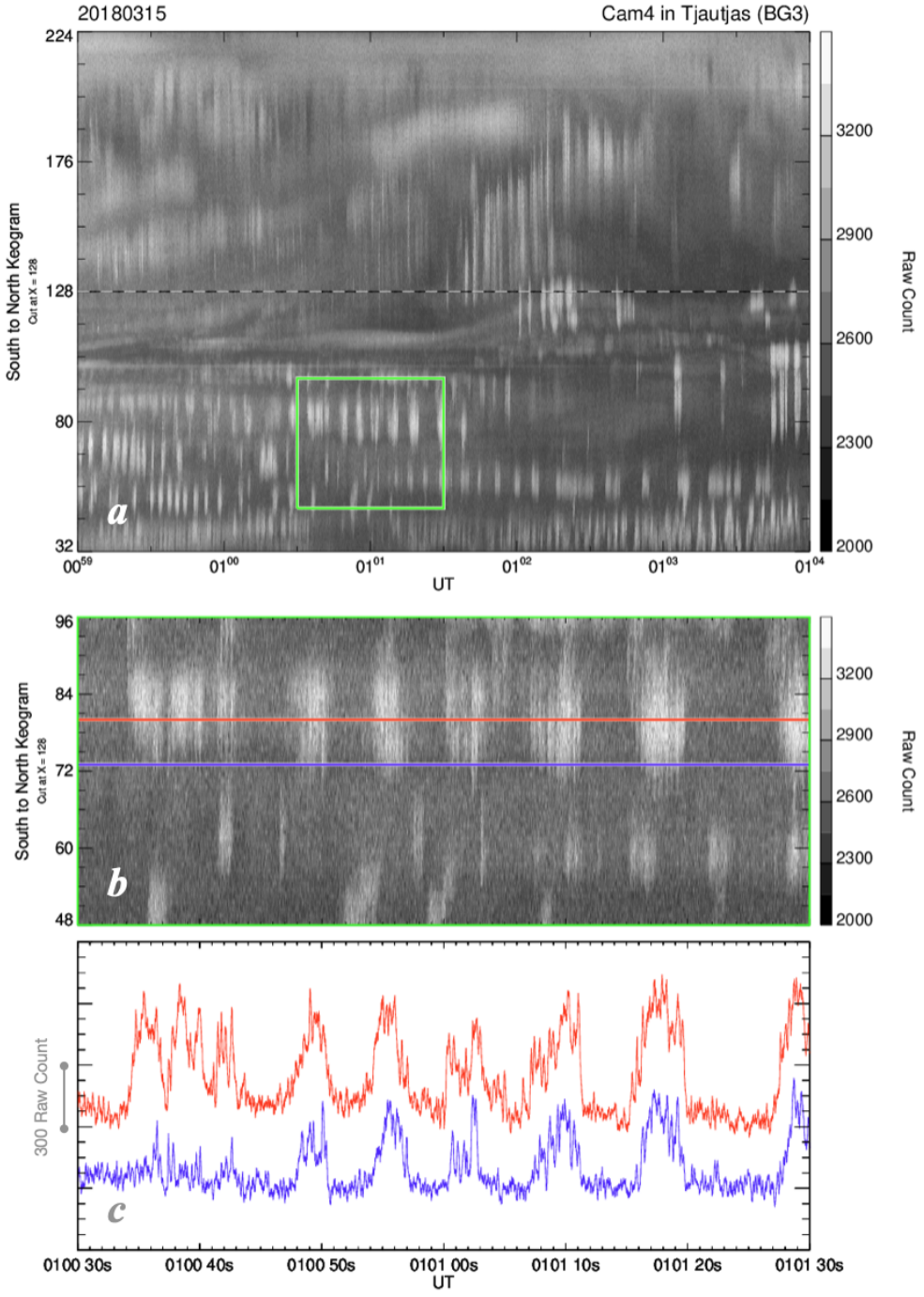

Figure 6: Temporal variations of PsA obtained by the 100-Hz ASI in Tjautjas, Sweden during the interval of simultaneous observations of PsA in Scandinavia on March 15, 2018, **(a)** the time-series of optical data from 00:59 to 01:04 UT in a format of south to north keogram, **(b)** zoom-in view of the 1-min optical data within the green box in the southern half of Figure 6a, **(c)** two time-series of the raw count sampled along the red and blue lines in Figure 6b.

One of the primary purposes of the current observations is to conduct ground-satellite conjugate observations of PsA, especially simultaneous measurements with the Arase spacecraft, which was launched in December 2016. The wave instruments onboard Arase, the Plasma Wave Experiment (PWE) (Kasahara et. al., 2018), are capable of so-called "burst mode operation" with 64 kHz sampling rate in limited time intervals (Matsuda et al., 2018). To find good intervals for simultaneous observations using the burst mode, we made a website showing conjunctions between the FOVs of various ground-based instruments at high-latitudes and the magnetic footprints of Arase. The website (https://ergsc.isee.nagoya-u.ac.jp/psa-gnd/bin/cif.cgi), which is called Conjunction Interval Finder (CIF), has been operative at the ERG Science Center at Nagoya University (Miyoshi et al., 2018b) since the start of the routine observation of Arase.

Figure 7 shows how CIF provides information about the conjunctions. In the top row, conjunctions between Arase and stations at the auroral latitudes (Scandinavia, Iceland, Antarctic Syowa Station, Alaska and Kola Peninsula in Russia) are displayed. In the middle two rows, conjunctions at the subauroral latitudes (most of them are the PWING sites) are shown. In the bottom row, conjunctions with the incoherent scatter radars (EISCAT, Kharkiv, PFISR, Millstone Hill and PANSY) are shown. In all the panels, the magnetic footprints of Arase derived by tracing the IGRF magnetic field lines are plotted where the color of the points represents MLT of the footprint. That is, bluish footprints mean morning side observations (00-06 MLT), which is favorable for the studies of PsA.

The satellite positioning data (predicted orbit data) and corresponding plots are refreshed every day. This website also offers a capability of showing plots from

previous/future periods. Users can browse the interval of their interest by specifying the date on top of the page. This will further enable the users to check the conjunctions for the interval of their interest but also for considering the timing of burst mode operation of the satellite.

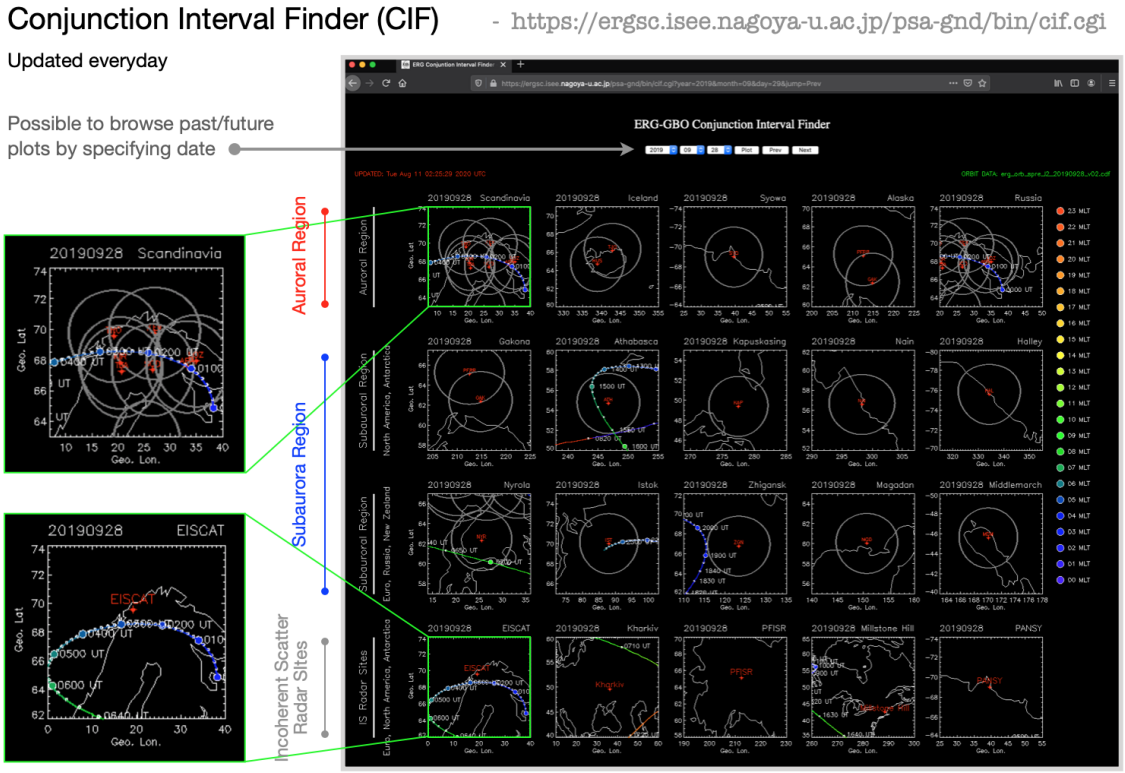

Figure 7: Conjunction Interval Finder (CIF) operated by the ERG Science Center at Nagoya University (https://ergsc.isee.nagoya-u.ac.jp/psa-gnd/bin/cif.cgi).

By listing up good conjunction intervals at CIF, we have operated the PWE WFC/OFA (Wave Form Capture/Onboard Frequency Analyzer) with the burst mode operation (Matsuda et al., 2018). Here we introduce one of such conjunction intervals of PsA in Scandinavia during 00-02 UT on March 29, 2017, which was captured just after

the start of the routine operation of Arase. Throughout this 2-hour interval, we measured very intense PsA within the FOVs of the ASIs in Sodankylä and Kevo in Finland. The magnetic footprint of Arase, calculated by the Tsyganenko 2004 model driven by the upstream solar wind conditions, stayed in the region of PsA for about 2 hours. Figure 8a and 8b are the frequency-time diagrams of PWE/OFA data (electric field and magnetic field) from Arase. We can identify a continuous activity of lower-band chorus throughout the interval in a frequency range from ~0.5 to 1 kHz.

To compare these optical data with the wave data from Arase, first we sampled the optical data from Sodankylä along the south to north cross section including the instantaneous footprint of Arase, and made some special keogram for the analysis of this conjunction. Figure 8c shows the special keogram where the vertical axis is south to north cross section at the instantaneous footprint of Arase, which is shown by the green horizontal curve. We see many vertical stripes which are typical signatures of PsA in the keogram. In the middle of this 2 hours interval, some parts of the optical data are saturated, but we can identify a continuous activity of PsA throughout the interval which is basically consistent with the long-lasting appearance of chorus waves in the top two panels. Figures 8d-f are zoom-in views of the first 20 min data in Figures 8a-c. Now it is clearly seen that the repetitive bursts of chorus waves (Figures 8d-e) are highly synchronized with the main pulsation of PsA in Figure 8f. Detailed analyses of the correlation of the main pulsation and internal modulation of PsA with the fine-scale temporal variation of chorus detected with Arase have already been reported by Kasahara et al. (2018), Ozaki et al. (2018), Kawamura et al. (2019) and Hosokawa et al. (2020) in detail.

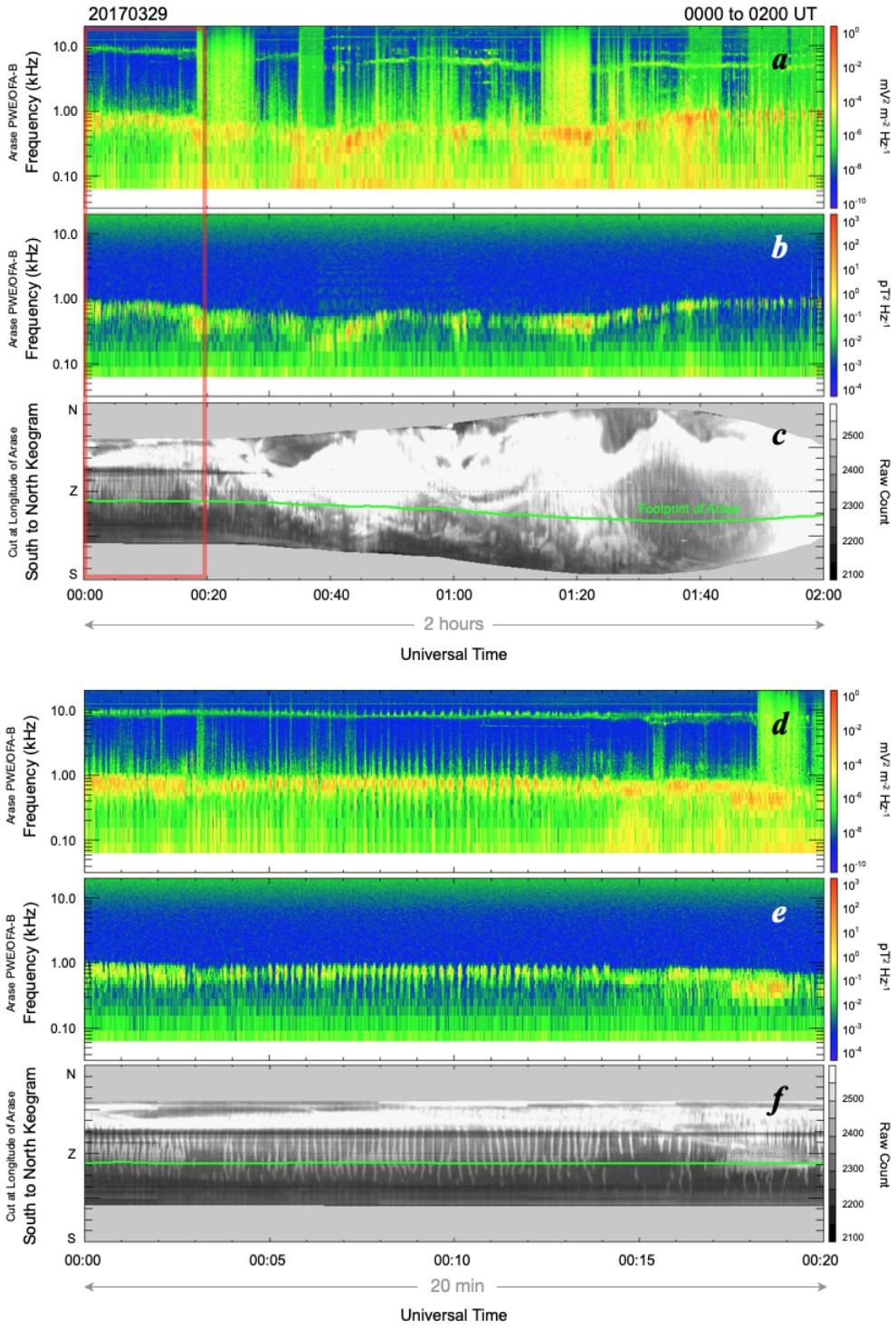

Figure 8: Conjugate observations of PsA and chorus on March 29, 2017. (a,b) frequency-time diagrams of PWE/OFA data from Arase. (c) optical data from Sodankylä along the south to north cross section including the instantaneous footprint of Arase. The footprint of Arase is traced by the horizontal green line. (d-f) zoom-in view of the first 20 min of Figures 8a-c.

3.2 Example of multi-wavelength observations

Figure 9 summarizes an example of multi-spectral observations of PsA during a 5 min interval from 0322 to 0327 UT on March 6, 2017. In this interval, two auroral emissions at 844.6 nm (Figures 9a and 9b) and 427.8 nm (Figures 9c and 9d) were observed respectively by two identical ASI systems with a temporal resolution of 10 Hz. The original raw count data have been converted to Rayleigh through the procedure described in section 2.2. In the keograms of both emissions, weak vertical stripes are seen which are manifestations of the main pulsation of PsA. Figures 9b and 9d respectively show the time-series of optical intensity at the horizontal red/blue lines in the keogram. To derive these time-series, the original 10-Hz data are spatially averaged with 3 x 3 spatial window and moving average with an window of 1 sec. This spatial/temporal averaging process makes the main pulsation of PsA visible through reduction of unwanted random noise. Important point is that the 10-Hz monochromatic ASI observations were able to detect the main pulsation of PsA in both the 427.8 and 844.6 nm emissions. This combination will enable us to estimate the energy of precipitation electrons during the ON and OFF phases of PsA by using a method introduced by Ono (1993) or by comparing the data with those estimated by the optical emission model such as GLOW (Solomon et al., 2017). Unfortunately, however, mainly due to the low S/N ratio of the 10-Hz sampling raw data, it would be difficult to extract the 3Hz internal modulation of PsA in the monochromatic ASI observations, especially for the dimmer 844.6 nm emission.

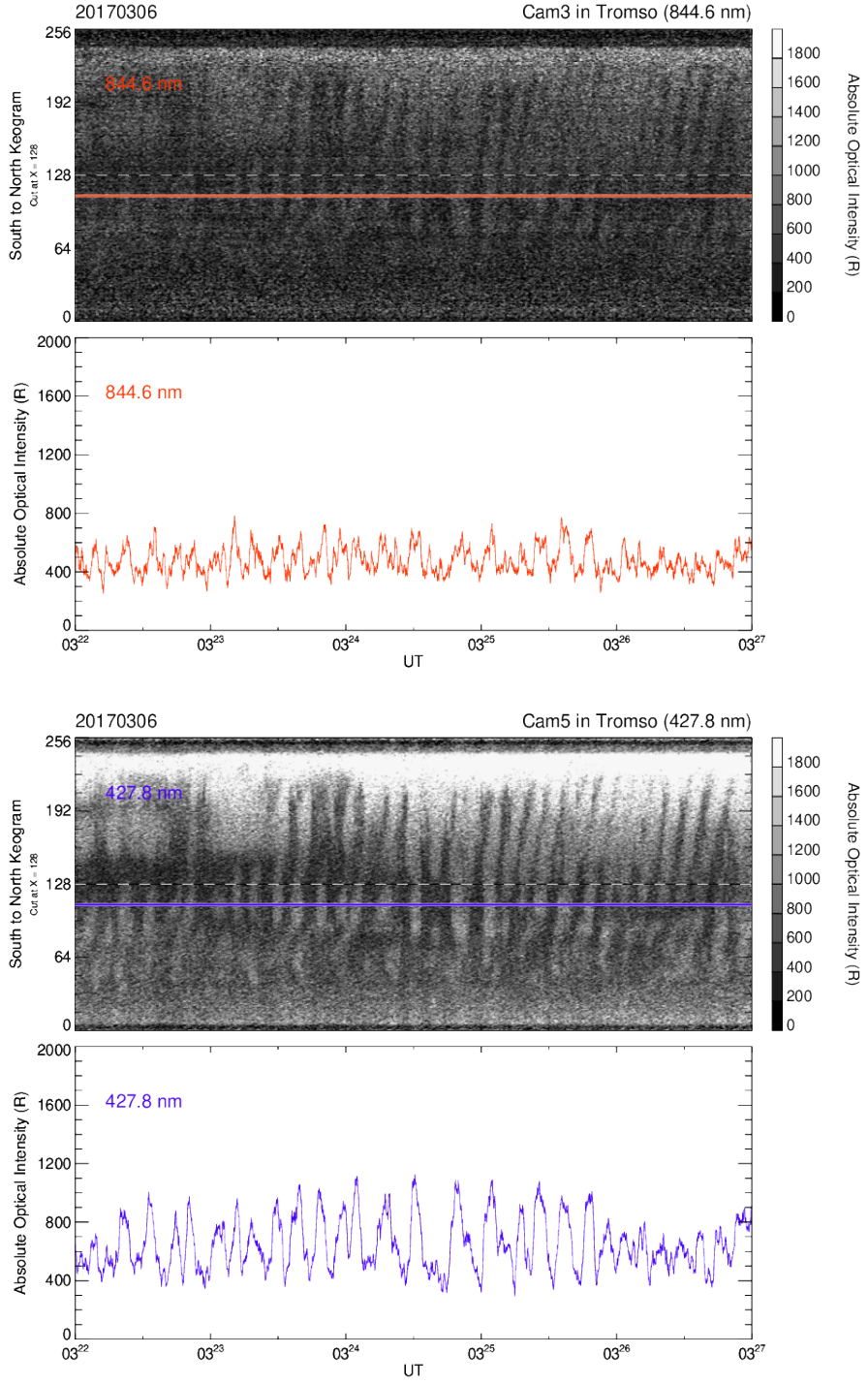

Figure 9: 10-Hz Monochromatic ASI observations during a 5 min interval from 03:22 to 03:27 UT on March 6, 2017. **(a,c)** south to north keogram of 844.6 and 427.8 nm emissions, **(b,d)** time-series of the optical intensity at the horizontal lines in the keogram.

The energy of precipitating electrons causing PsA is one of the fundamental parameters characterizing the process of wave particle interaction (WPI). For example, the energy of PsA electrons can be used to infer the resonance energy of the first-order cyclotron resonance (Kennel and Petscheck, 1966). The information about the energy can also be used for determining how far the region of WPI is located away from the magnetic equator (Miyoshi et al., 2010, 2015b, 2020). We might be able to observe a systematic change in the characteristic energy of electrons during a single pulse of PsA, which can be interpreted by the time-of-flight effect of precipitating electrons (e.g., Miyoshi et al., 2010, 2015b, 2020). In those senses, it is of particular importance in the studies of PsA to estimate the characteristic energy of electrons using the two wavelengths method.

An alternative approach for estimating the energy of auroral electrons is realized by the MAIN (Multiscal Auroral Imaging Network) system in Apatity, Kola Peninsula (Kozelov et al., 2012; 2013). Two identical cameras are operated with a separation of 4.12 km. The cameras are equipped wtih glass filters which cut the slowest red-line emission. The cameras are directed to the magnetic zenith and synchronously observe auroral structures in a 10ox15o field-of-view with a temporal resolution of 1 s. Short separation distance between the cameras allows us to avoid problems when identifying the auroral structures for longer separation case. This displacement gives us an estimation of the emission height, which can be converted to the average energy of precipitating electrons. This algorithm will work well for PsA whose vertical thickness is relatively small.

In recent years, several studies have indicated that the energy of PsA electrons becomes harder in the morning side (Hosokawa and Ogawa, 2015; Partamies et al., 2017; Kawamura et al., 2020). It is also expected that the energy of PsA electrons depends on

the morphology of optical signature of PsA (Oyama et al., 2017, Grono and Donovan, 2018, 2020). To answer these questions, it is highly demanded to estimate the characteristic energy of PsA electrons as an all-sky map. It is rather difficult to derive such an energy map, especially near the edge of the field-of-view, because the difference in the altitude of 427.8 and 844.6 nm emissions and the oblique viewing geometry introduce a spatial displacement between the two different emissions. By using the data obtained by a pair of monochromatic ASIs, we will address these issues and clarify the limitation in the 2D mapping of the energy of precipitating electrons.

3.3 Optical, radar and geomag observations of PsA in Tromsø

Here, we introduce an integrated observation of PsA by combining data from the ground-based ASIs, magnetometer and EISCAT radar in Tromsø, Norway. On the night of February 17, 2018, we conducted a campaign observation of PsA by using the EISCAT UHF radar in combination with EMCCD ASIs and magnetometer in Tromsø. Figure 10 shows a summary of the measurements during a 10 min interval from 02:10 to 02:20 UT. The top panel shows the 100-Hz ASI data in the format of south to north keogram where the horizontal dashed line shows the position of the field-aligned beam of the CP1 observation mode of EISCAT UHF radar. The keogram well demonstrates successive appearances of stripes in the vicinity of the sensing area of EISCAT which are manifestations of the main pulsation of PsA. Figure 10b shows the altitude-time plot of the electron density obtained from the EISCAT UHF radar. The electron density in the E region altitude (say from 90 to 120 km) exhibits a characteristic modulation, which corresponds to the optical pulsation seen in Figure 10a. The bottom two panels of Figure 10 respectively display the residual of the X (northward) and Y (eastward) components

of ground-based magnetic field observations. The comparison with the optical and electron density data indicates that the X (Y) component decreases (increases) when PsA becomes ON. The other thing worth noting is that the coherent magnetic field variation is more clearly seen in the Y component (eastward component), which is consistent with recent observations by Mitchell and Samara (2015). In particular, the Y component of the magnetic field becomes eastward during the ON phase of PsA.

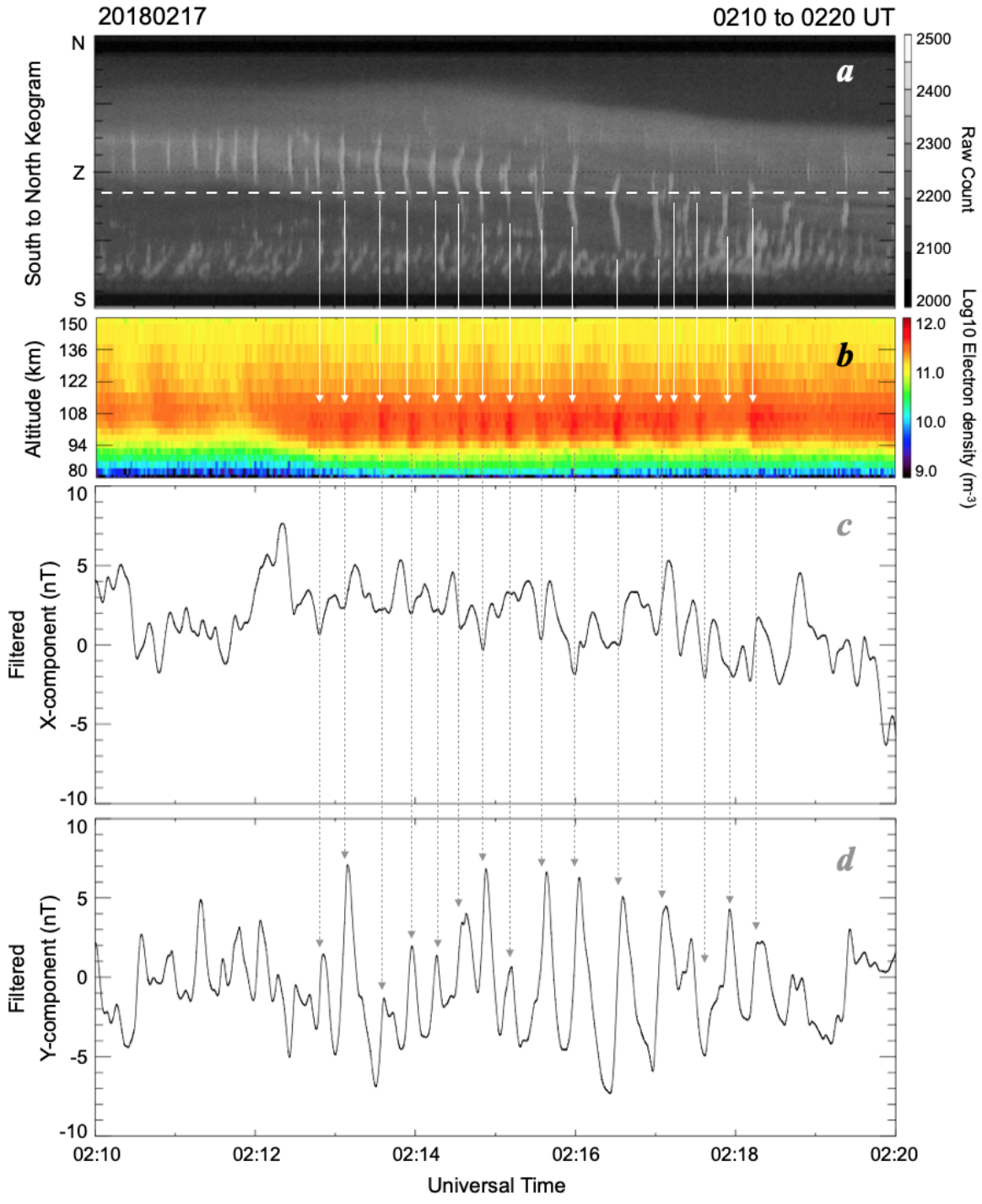

Figure 10: Simultaneous optical, electron density and magnetic field observations in Tromsø, Norway on February 17, 2018. **(a)** south to north keogram made from the 100-Hz ASI images where the sensing area of the EISCAT UHF radar (field-aligned direction) is drawn with the horizontal dashed line. **(b)** altitude-time plot of electron density from EISCAT, **(c, d)** residual of the X and Y component of magnetic field in Tromsø.

As shown in Figure 10, coherent magnetic field pulsation was seen during the interval of PsA. The EISCAT radar, at the same time, identified a variation in the electron density showing similar periodic signatures. These simultaneous observations confirm the origin of magnetic field pulsation during PsA. First the temporal variation in the flux of electron precipitation during PsA produces a pulsation in the electron density. The pulsation in the electron density then modulates the ionospheric current flowing in the horizontal direction through changes in the conductance. Eventually, modified ionospheric current generates pulsation in the magnetic field on the ground. This idea was initially implied by Arnoldy et al. (1982), Oguti and Hayashi (1984) and Oguti (1986), but it has been difficult to prove it by comparing simultaneous observations of the optical intensity, electron density, and ground magnetic field with sufficiently high temporal resolution. The current finding was obtained because we operate the optical instruments and ground-based magnetometer both of which can detect sub-second variations of PsA and ionospheric currents. This clearly indicates that the current combination of high-time resolution optical and magnetic field observations can be used to investigate the change of ionospheric current system (and possible closure of current) during the episodes of PsA (i.e., ON and OFF phases of the main pulsation) following a mechanism for example discussed by Hosokawa et al. (2010).

4. Summary and Discussion

We have developed and deployed a set of scientific equipment for studying pulsating aurora. The system is composed of the following instruments:

1. High-speed EMCCD ASIs at 100 Hz sampling at 6 stations in Scandinavia and Alaska
2. Two monochromatic EMCCD ASIs at 10 Hz sampling rate in Tromsø, which mainly observe the 427.8 nm and 844.6 nm emissions
3. Multiple monochromatic Watec ASIs at 6 stations
4. A 5-channel photometer in Tromsø, which can be used for calibration of the monochromatic ASIs
5. A 20-Hz sampling ground-based fluxgate magnetometer in Tromsø

The six high-speed EMCCD ASIs are mainly used for visualizing the fine-scale temporal characteristics of PsA in a wide area, especially during conjunction observations of the Arase satellite. The monochromatic ASI systems are used for estimating the energy of precipitating PsA electrons in 2D with a support of 5-channel photometer as a calibration standard. The high-time resolution fluxgate magnetometer will be intensively used for observing rapid changes in the ionospheric current system during the ON/OFF phases of PsA in combination with simultaneous observations of the ionospheric electron density (i.e., conductance) by the EISCAT radar in Tromsø.

The raw data files from the 100-Hz EMCCD ASIs are downloadable from a site at https://ergsc.isee.nagoya-u.ac.jp/psa-gnd/pub/raw within the ERG Science Center. The software written in IDL (Interactive Data Language) for reading and plotting the raw data files is also available at https://ergsc.isee.nagoya-u.ac.jp/psa-gnd/pub/raw/soft/. The software can run with/without SPEDAS (Space Physics Environment Data Analysis

System: Angelopoulos et al., 2019) environment. CDF format data files with a temporal resolution of 10 Hz are currently being produced from the original 100-Hz raw data. The 10-Hz CDF format data (including 20-Hz photometer data) will become downloadable at https://ergsc.isee.nagoya-u.ac.jp/psa-gnd/pub/cdf/. All the data for quick look are available at https://ergsc.isee.nagoya-u.ac.jp/psa-gnd/bin/psa.cgi, where keograms and digest movies can be browsed. The detailed information about the quality of the ASIs (both 100 Hz and 10 Hz) and magnetometer data is described and regularly updadated at https://ergsc.isee.nagoya-u.ac.jp/psa-gnd/pub/raw/operation_note.txt.

Continuous efforts will be taken to keep the entire PsA observation system operative during the next solar cycles. The high-speed 100-Hz ASI data have been used for conjunction measurements with the Arase satellite (e.g., Fukizawa et al., 2018; Ozaki et al., 2019; Hosokawa et al., 2020). Good conjunction is still expected in the coming 2020-2021 winter season in the northern hemisphere. Not only in the northern hemisphere, there are a few high-speed auroral cameras operative in Antarctica, at the Japanese Syowa station. Collaboration with Arase and other ground-based optical instruments will provide additional chances to investigate the detailed characteristics of PsA. We plan to launch a sounding rocket for observing PsA in an in-situ manner during the winter of 2021. The rocket will be launched from the Polar Flat Research Range in Fairbanks, Alaska, at which one of the 100-Hz high-speed ASIs has been operative. At the time of the rocket campaign, 100-Hz high-speed 2D images of PsA will be used for obtaining the background status of regions of PsA through which the rocket will fly.

Now EISCAT_3D system (e.g., McCrea et al., 2015) is being constructed in northern Scandinavia, which will be the largest incoherent scatter radar system in the world when fully operated. At least 3 high-speed ASIs have a common FOV with the

core-site antenna at Skibotn, Norway. The EISCAT_3D will provide high-time resolution data of electron density and ion velocity in 3D, which will be compared with the high-speed optical data in the surrounding area. In the framework of the collaboration with EISCAT_3D, targets of measurements are not only PsA but also other kinds of aurora such as discrete aurora and flickering aurora. Not only the collaboration with EISCAT_3D, collaboration with other existing radio observation systems such as PFISR, KAIRA (McKay et al., 2015), Riometers and VLF measurements to detect whistler waves as well as to measure the standard radio waves are particularly important for comprehensive analyses of PsA, which have been demonstrated for several analysis about PsA (Ozaki et al., 2015; Grandin et al., 2017; Tsuchiya et al., 2018).

In recent years, high-energy electron precipitation (EEP), especially during intervals of PsA, has been focused on because substantial ionization periodically appeared in the auroral zone. EEP with energy of 100 keV or higher can ionize the atmosphere at 80 km and lower. Same as the chemical reactions during solar proton events, increase of NOx and HOx leads to decrease of the ozone density at ionization heights (Turunen et al., 2016). EEPs capable of ionizing the upper mesosphere and lower frequently arise along with PsA (Hosokawa and Ogawa, 2015; Miyoshi et al., 2015b, 2020; Oyama et al., 2017), and simultaneous measurements of aurora and space plasma show that PsA is generated by interactions between plasma waves and energetic electrons in the magnetosphere (Kasahara et al., 2018; Ozaki et al., 2019; Hosokawa et al., 2020). Thus, in the future, it is also highly demanded to conduct combined/integrated measurements of ionosphere, magnetosphere and middle atmosphere during PsA since PsA is a phenomenon linking space plasma physics and atmospheric climatology.

Acknowledgements

K.H., S.O., Y.O. Y.M. and R.F. are supported by JSPS Kakenhi (15H05747). Y.M. and R.K. are supported by JSPS Kakenhi (15H05815). S.O., Y.M., S.K., R.K. and K.S. are supported by JSPS Kakenhi (16H06286). K.H., Y.M. and S.K. are supported by the International Space Science Institutes Beijing (ISSI-BJ) International Team program. Y.M., S.K., and Y. K. are supported by JSPS Bilateral Open Partnership Joint Research Projects. K.H., S.O., Y.M., Y.K., K.S. and I.S. are supported by JSPS Bilateral Open Partnership Joint Research Projects (JPJSBP120194814). Y.K. is supported by JSPS Kakenhi (16H04056 and 16H01172). The data from the Arase (ERG) satellite and ground-based instruments were obtained from the ERG Science Center operated by the Institute of Space and Astronautical Science of the Japan Aerospace eXploration Agency and the Institute for Space-Earth Environmental Research of Nagoya University (https://ergsc.isee.nagoya-u.ac.jp/index.shtml.en, Miyoshi et al., 2018b). In the present study, we used level 2 OFA v02.01. The operation of the instruments in Tromsø has been supported by TGO, the Arctic University of Norway (UiT). The operation of the instruments in Tromsø has been supported by the Arctic University of Norway (UiT). The operation of the ASIs in Sodankylä has been supported by the Sodankylä Geophysical Observatory (SGO). The operation of the ASIs in Tjautjas has been supported by the Swidesh Institute of Space Physics (IRF). The operation of the EMCCD ASI in Kevo has been supported by the Finnish Meteorological Institute (FMI) and Turku University. The operation of the EMCCD ASIs in Gakona and Poker Flat Research Range, Alaska, has been supported by the University of Alaska Fairbanks (UAF).

References

Angelopoulos, V., P. Cruce, A. Drozdov, et al. (2019), The Space Physics Environment Data Analysis System (SPEDAS), Space Sci. Rev., 215, 9, https://doi.org/10.1007/s11214-018-0576-4.

Arnoldy, R. L., K. Dragoon, L. J. Cahill, S. B. M. Jr., and T. J. Rosenberg (1982), Detailed correlations of magnetic field and riometer observations at L = 4.2 with pulsating aurora, J. Geophys. Res., 87, 10,449–10,456, doi:10.1029/JA087iA12p10449.

Baker, K. B., and S. Wing (1989), A new magnetic coordinate system for conjugate studies of high latitudes, J. Geophys. Res., 94, 9139.

Duncan, C. N., et al. (1981), Latitudinal and temporal characteristics of pulsating auroras, Can. J. Phys., 59, 1063–1069.

Ebihara, Y., T. Ikeda, Y. Omura, T. Tanaka, & M.-C. Fok (2020), Nonlinear wave growth analysis of whistler-mode chorus generation regions based on coupled MHD and advection simulation of the inner magnetosphere, Journal of Geophysical Research: Space Physics, 125, e2019JA026951.

Feldsten, Y. I., and G. V. Starkov (1967), Dynamics of auroral belt and polar geomagnetic disturbance, Planet. Space Sci., 15, 209–229, doi:10.1016/0032-0633(67)90190-0.

Ebihara, Y., T. Ikeda, Y. Omura, T. Tanaka, & M.-C. Fok (2020), Nonlinear wave growth analysis of whistler-mode chorus generation regions based on coupled

MHD and advection simulation of the inner magnetosphere, Journal of Geophysical Research: Space Physics, 125, e2019JA026951.

Foster, J. C., & T. J. Rosenberg (1976), Electron precipitation and VLF emissions associated with cyclotron resonance interactions near the plasmapause. Journal of Geophysical Research, 81(13), 2183–2192.

Foster, J. C., P. J. Erickson, Y. Omura, D. N. Baker, C. A. Kletzing, & S. G. Claudepierre (2017), Van Allen Probes observations of prompt MeV radiation belt electron acceleration in nonlinear interactions with VLF chorus, Journal of Geophysical Research: Space Physics, 122, 324–339.

Fukizawa, M., T. Sakanoi, Y. Miyoshi, K. Hosokawa, K. Shiokawa, Y. Katoh, et al. (2018), Electrostatic electron cyclotron harmonic waves as a candidate to cause pulsating auroras, Geophysical Research Letters, 45, 12,661-12,668. https://doi.org/10.1029/2018GL080145.

Grandin, M. A., A. Kero, N. Partamies, D. McKay, D. Whiter, A. Kozlovsky, and Y. Miyoshi (2017), Observation of pulsating aurora signature in cosmic noise absorption data, Geophys. Res. Lett., 44, 5292-5300, doi:10.1002/2017GL073901.

Grono, E. and E. Donovan (2018), Differentiating diffuse auroras based on phenomenology, Ann. Geophys., 36, 891–898, https://doi.org/10.5194/angeo-36-891-2018.

Grono, E. and E. Donovan (2020), Surveying pulsating auroras, Ann. Geophys., 38, 1–

8, https://doi.org/10.5194/angeo-38-1-2020, 2020..

Hosokawa, K., and Y. Ogawa (2015), Ionospheric variation during pulsating aurora, J. Geophys. Res. Space Physics, 120, 5943–5957, doi:10.1002/2015JA021401.

Hosokawa, K., Y. Miyoshi, and W. Li (2015), Introduction to special section on pulsating aurora and related magnetospheric phenomena, Journal of Geophysical Research Space Physics, 120, 5341-5343. doi:10.1002/2015JA021453.

Hosokawa, K., Y. Miyoshi, M. Ozaki, S.-I. Oyama, Y. Ogawa, S. Kurita, Y. Kasahara, Y. Kasaba, S. Yagitani, S. Matsuda, F. Tsuchiya, A. Kumamoto, R. Kataoka, K. Shiokawa, T. Raita, E. Turunen, T. Takashima, I. Shinohara and R. Fujii (2020), Multiple time-scale beats in aurora: precise orchestration via magnetospheric chorus waves, Nature Sci. Rep., 10, 3380, https://doi.org/10.1038/s41598-020-59642-8.

Jones, A. V. (1974) , Aurora, Reidel Publishing Company, Dordrecht, doi:10.1007/978-94-010-2099-2.

Kasahara, S. et al. (2018), Pulsating aurora from electron scattering by chorus waves, Nature, 554, 337–340.

Kasahara, Y. et al. (2018), The plasma wave experiment (PWE) on board the Arase (ERG) satellite, Earth, Planets and Space, 70, doi:10.1186/s40623-018-0842-4.

Kataoka, R., Y. Miyoshi, D. Hampton, T. Ishii, and H. Kozako (2012), Pulsating aurora beyond the ultra-low frequency range, Journal of Geophysical Research, 117, A08336, doi:10.1029/2012JA017987.

Katoh, Y., & Y. Omura (2007), Computer simulation of chorus wave generation in the Earth's inner magnetosphere, Geophysical Research Letters, 34, L03102.

Kawamura, Y., K. Hosokawa, S. Nozawa, et al. (2020), Estimation of the emission altitude of pulsating aurora using the five-wavelength photometer, Earth, Planets Space, 72, 96, https://doi.org/10.1186/s40623-020-01229-8.

Kennel C. F. and H. E. Petschek (1966), Limit on stably trapped particle fluxes, J. Geophys. Res., 71, 1–28, https://doi.org/10.1029/JZ071i001p00001.

Kozelov, B. V., S. V. Pilgaev, L. P. Borovkov, and V. E. Yurov (2012), Multi-scale auroral observations in Apatity: winter 2010–2011, Geosci. Instrum. Method. Data Syst., 1, 1–6, https://doi.org/10.5194/gi-1-1-2012.

Kozelov, B. V., B. U. E. Brändström, F. Sigernes, A. V. Roldugin, and S.A. Chernouss (2013), Practice of CCD cameras' calibration by LED low-light source. "Physics of Auroral Phenomena". Proc. of 36-th Annual Seminar. Apatity. 151–154.

Lanchester, B. S., J. R. Palmer, M. H. Rees, D. Lummerzheim, K. Kaila, and T. Turunen (1994), Energy flux and characteristic energy of an elemental auroral structure, Geophys. Res. Lett., 21, 2789–2792.

Lessard, M. (2012), A review of pulsating aurora, in Auroral Phenomenology and Magnetospheric Processes: Earth And Other Planets (eds A. Keiling, E. Donovan, F. Bagenal and T. Karlsson), AGU monograph series, 197, doi:10.1029/2011GM001187.

Matsuda, S., Y. Kasahara, H. Kojima, Y. Kasaba, S. Yagitani, M. Ozaki, T. Imachi, K.

Ishisaka, A. Kumamoto, F. Tsuchiya, M. Ota, S. Kurita, Y. Miyoshi, M. Hikishima, A Matsuoka, and I. Shinohara (2018), Onboard Software of Plasma Wave Experiment aboard Arase: Instrument Management and Signal Processing of Waveform Capture/Onboard Frequency Analyzer, Earth, Planets and Space, 70:75, doi:10.1186/s40623-018-0838-0.

McCrea, I. W., A. Aikio, L. Alfonsi, E. Belova, S. Buchert, M. Clilverd, N. Engler, B. Gustavsson, C. Heinselman, J. Kero, M. Kosch, H. Lamy, T. Leyser, Y. Ogawa, K. Oksavik, A. Pellinen-Wannberg, F. Pitout, M. Rapp, I. Stanislawska, J. Vierninen (2015), The science case for the EISCAT_3D radar, Progress in Earth and Planetary Science, doi:10.1186/s40645-015-0051-8.

McKay, D., R. Fallows, M. Norden, A. Aikio, J. Vierinen, F. Honary, S. Marple, and T. Ulich (2015), All-sky interferometric riometry, Radio Sci., 50, 1050-1061, doi:10.1002/2015RS005709.

Mende, S. B., S. E. Harris, H. U. Frey, et al. (2008), The THEMIS Array of Ground-based Observatories for the Study of Auroral Substorms, Space. Sci. Rev., 141, 357, https://doi.org/10.1007/s11214-008-9380-x.

Michell, R. G., and M. Samara (2015), Ground magnetic field fluctuations associated with pulsating aurora, J. Geophys. Res. Space Physics, 120, 9192– 9201, doi:10.1002/2015JA021252.

Miyoshi, Y., Y. Katoh, T. Nishiyama, T. Sakanoi, K. Asamura, and M. Hirahara (2010), Time of flight analysis of pulsating aurora electrons, considering wave-particle interactions with propagating whistler mode waves, J. Geophys. Res.,

115, A10312, doi:10.1029/2009JA015127.

Miyoshi, Y., S. Saito, K.Seki, T. Nishiyama, R. Kataoka, K. Asamura, Y. Katoh, Y. Ebihara, T. Sakanoi, M. Hirahara, S. Oyama, S. Kurita, and O. Santolik (2015a), Relation between energy spectra of pulsating aurora electrons and frequency spectra of whistler-mode chorus waves, J. Geophys. Res., 120, 7728-7736, doi:10.1002/2015JA021562.

Miyoshi, Y., S. Oyama, S. Saito, S. Kurita, H. Fujiwara, R. Kataoka, Y. Ebihara, C. Kletzing, G. Reeves, O. Santolik, M. Clilverd, C. J. Rodger, E. Turunen, and F. Tsuchiya (2015b), Energetic electron precipitation associated with pulsating aurora: EISCAT and Van Allen Probe observations. J. Geophys. Res. Space Physics, 120, 2754–2766, doi: 10.1002/2014JA020690.

Miyoshi Y, I. Shinohara, T. Takashima, K. Asamura, N. Higashio, T. Mitani, S. Kasahara, S. Yokota, Y. Kazama, S.-Y. Wang, SW Tam, PTPT Ho, Y. Kasahara, Y. Kasaba, S. Yagitani, A. Matsuoka, H. Kojima, Y. Katoh, K. Shiokawa, and K. Seki (2018a), Geospace Exploration Project ERG, Earth Planets Space, 70:101, doi:10.1186/s40623-018-0862-0.

Miyoshi, Y., T. Hori, M. Shoji, M. Teramoto, T-F. Chang, T. Segawa, N. Umemura, S. Matsuda, S. Kurita, K. Keika, Y. Miyashita, K. Seki, Y. Tanaka, N. Nishitani, S. Kasahara, S. Yokota, A. Matsuoka, Y. Kasahara, K. Asamura, T. Takashima, and I. Shinohara (2018b), The ERG Science Center, Earth, Planets, Space., 70:96, doi:10.1186/s40623-018-0867-8.

Miyoshi, Y., S. Saito, S. Kurita, K. Asamura, K. Hosokawa, T. Sakanoi, T. Mitani, Y.

Ogawa, S. Oyama, F. Tsuchiya, S. L. Jones, A. N. Jaynes, and J. B. Blake (2020), Relativistic electron microbursts as high energy tail of pulsating aurora electrons, Geophys. Res. Lett., e2020GL090360, doi:10.1029/2020GL090360.

Nakajima, A., et al. (2012), Electron and wave characteristics observed by the THEMIS satellites near the magnetic equator during a pulsating aurora, J. Geophys. Res., 117, A03219, doi:10.1029/2011JA017066.

Nishimura, Y., et al. (2010), Identifying the driver of pulsating aurora, Science, 330, 81-84.

Nishimura, Y., M. R. Lessard, Y. Katoh, et al. (2020), Diffuse and Pulsating Aurora, Space Sci. Rev., 216, 4, https://doi.org/10.1007/s11214-019-0629-3.

Nishiyama, T., T. Sakanoi, Y. Miyoshi, Y. Katoh, K. Asamura, S. Okano, and M. Hirahara (2011), The source region and its characteristic of pulsating aurora based on the Reimei observations, J. Geophys. Res., 116, A03226, doi:10.1029/2010JA015507

Nishiyama, T., Y. Miyoshi, Y. Katoh, T. Sakanoi, R. Kataoka, and S. Okano (2016), Substructures with luminosity modulation and horizontal oscillation in pulsating patch: Principal component analysis application to pulsating aurora, J. Geophys. Res. Space Physics, 121, 2360– 2373, doi:10.1002/2015JA022288.

Nozawa, S., T. Kawabata, K. Hosokawa, et al. (2018), A new five-wavelength photometer operated in Tromsø (69.6°N, 19.2°E), Earth, Planets Space, 70, 193, https://doi.org/10.1186/s40623-018-0962-x.

Nunn, D. (1974), A self-consistent theory of triggered VLF emissions, Planetary and Space Science, 22(3), 349–378.

Ogawa, Y., Y. Tanaka, A. Kadokura, K. Hosokawa, Y. Ebihara, T. Motoba, B. Gustavsson, U. Brändström, Y. Sato, S. Oyama, M. Ozaki, T. Raita, F. Sigernes, S. Nozawa, K. Shiokawa, M. Kosch, K. Kauristi, C. Hall, S. Suzuki, Y. Miyoshi, A. Gerrard, H. Miyaoka, and R. Fujii (2020a), Development of low-cost multi-wavelength imager system for studies of aurora and airglow, Polar Science, 23, 100501, https://doi.org/10.1016/j.polar.2019.100501.

Ogawa, Y., A. Kadokura, and M. K. Ejiri (2020b), Optical calibration system of NIPR for aurora and airglow observations, Polar Science, 100570, doi: 10.1016/j.polar.2020.100570.

Oguti, T., and K. Hayashi (1984), Multiple correlation between auroral and magnetic pulsations. II - Determination of electric currents and electric fields around a pulsating auroral patch, J. Geophys. Res., 89, 7467–7481, doi:10.1029/JA089iA09p07467.

Oguti, T., K. Hayashi, T. Yamamoto, J. Ishida, T. Higuchi, and N. Nishitani (1986), Absence of hydromagnetic waves in the magnetospheric equatorial region conjugate with pulsating auroras, J. Geophys. Res., 91(A12), 13711–13715, doi:10.1029/JA091iA12p13711.

Omura, Y., Y. Katoh, & D. Summers (2008), Theory and simulation of the generation of whistler-mode chorus, Journal of Geophysical Research, 113, A04223.

Omura, Y., D. Nunn, & D. Summers (2013), Generation processes of whistler mode chorus emissions: Current status of nonlinear wave growth theory, In D. Summers, I. R. Mann, D. N. Baker, & M. Schulz (Eds.), Dynamics of the Earth's Radiation Belts and Inner Magnetosphere (pp. 243–254). Washington DC: American Geophysical Union.

Omura, Y., Y. Hsieh, J. C. Foster, P. J. Erickson, C. A. Kletzing, & D. N. Baker (2019), Cyclotron acceleration of relativistic electrons through Landau resonance with obliquely propagating whistler-mode chorus emissions, Journal of Geophysical Research: Space Physics, 124, 2795–2810.

Ono T. (1993), Derivation of energy parameters of precipitating auroral electrons by using the intensity ratios of auroral emissions, J. Geomagn. Geolectr., 45, 455–472.

Oyama, S., A. Kero, C. J. Rodger, M. A. Clilverd, Y. Miyoshi, N. Partamies, E. Turunen, T. Raita, P. T. Verronen, and S. Saito (2017), Energetic electron precipitation and auroral morphology at the substorm recovery phase, J. Geophys. Res. Space Physics, 122, doi:10.1002/2016JA023484.

Oyama, S., T. T., Tsuda, K. Hosokawa et al. (2018), Auroral molecular-emission effects on the atomic oxygen line at 777.4 nm, Earth, Planets Space, 70, 166, https://doi.org/10.1186/s40623-018-0936-z.

Ozaki, M., S. Yagitani , K. Sawai , K. Shiokawa , Y. Miyoshi , R. Kataoka , A. Ieda , Y. Ebihara , M. Connors , S. Ian , Y. Katoh , Y. Otsuka , N. Sunagawa , and V. Jordanova (2015), A direct link between chorus emissions and pulsating aurora on

timescales from milliseconds to minutes: A case study at subauroral latitudes, J. Geophys. Res., 120, 9617-9631, doi:10.1029/2015JA021381.

Ozaki, M., Y. Miyoshi, K. Shiokawa, K. Hosokawa, S. Oyama, R. Kataoka, Y. Ebihara, Y. Ogawa, Y. Kasahara, S. Yagitani, Y. Kasaba, A. Kumamoto, F. Tsuchiya, S. Matsuda, Y. Katoh, M. Hikishima, S. Kurita, Y. Otsuka, R. C. Moore, Y. Tanaka, M. Nosé, T. Nagatsuma, N. Nishitani, A. Kadokura, M. Connors, T. Inoue, A. Matsuoka, and I. Shinohara (2019), Visualization of rapid electron precipitation via chorus element wave–particle interactions, Nature Communications, doi:10.1038/s41467-018-07996-z.

Partamies, N., D. Whiter, A. Kadokura, K. Kauristie, H. Nesse Tyssoy, S. Massetti, P. Stauning, and T. Raita (2017), Occurrence and average behavior of pulsating aurora, J. Geophys. Res., doi:10.1002/2017JA024039.

Røyrvik, O. and T. N. Davis (1977), Pulsating aurora: Local and global morphology, Journal of Geophysical Research, 82, 4720-4740.

Roldugin, A. V., Z. V. Dashkevich, M. V. Kuznetsova, and Y. V. Fedorenko (2017), An all-sky camera for recording three auroral emissions. Instruments and Experimental Techniques, 60(2), 265–270. doi:10.1134/s0020441217020221.

Rosenberg, T. J., R. A. Helliwell, & J. P. Katsufrakis (1971), Electron precipitation associated with discrete very-low-frequency emissions, Journal of Geophysical Research, 76(34), 8445–8452.

Roux, A., & R. Pellat (1978), A theory of triggered emissions, Journal of Geophysical

Research, 83(A4), 1433.

Samara, M., and R. G. Michell (2010), Ground-based observations of diffuse auroral frequencies in the context of whistler mode chorus, J. Geophys. Res., 115, A00F18, doi:10.1029/2009JA014852.

Sandahl, I., L. Eliasson, and R. Lundin (1980), Rocket observations of precipitating electrons over a pulsating aurora, Geophysical Research Letters, 7, 309-312.

Shiokawa, K., Y. Katoh, Y. Hamaguchi et al. (2017), Ground-based instruments of the PWING project to investigate dynamics of the inner magnetosphere at subauroral latitudes as a part of the ERG-ground coordinated observation network, Earth, Planets Space, 69, 160, https://doi.org/10.1186/s40623-017-0745-9.

Solomon, S. C. (2017), Global modeling of thermospheric airglow in the far ultraviolet, J. Geophys. Res. Space Physics, 122, 7834–7848, doi:10.1002/2017JA024314.

Taguchi, M., M. Ejiri, and K. Tomimatsu (2004), A new all-sky optics for aurora and airglow imaging, Adv. Polar Upper Atmos. Res., 18, 140–148.

Thomas, R. W., and P. Rothwell (1979), A latitude effect in the periodicity of auroral pulsating patches, J. Atmos. Terr. Phys., 41, 1179–1184.

Tsuchiya, F., A. Hirai, T. Obara, H. Misawa, S. Kurita, Y. Miyoshi, K. Shiokawa, M. Connors, M. Ozaki, Y. Kasahara, A. Kumamoto, Y. Kasaba, A. Matsuoka, M. Shoji, and I. Shinohara (2018), Energetic electron precipitation associated with pulsating aurora observed by VLF radio propagation during the recovery phase of a substorm on 27 March 2017, Geophys. Res. Lett., 45, 12651–12660,

doi;10.1029/2018GL080222.

Turunen, E., A. Kero, P. T. Verronen, Y. Miyoshi, S.-I. Oyama, and S. Saito (2016), Mesospheric ozone destruction by high-energy electron precipitation associated with pulsating aurora, J. Geophys. Res. Atmos., 121, doi:10.1002/2016JD025015.

Yamamoto, T. (1988), On the temporal fluctuations of pulsating auroral luminosity, Journal of Geophysical Research, 93, 897–911, doi:10.1029/JA093iA02p00897.